Quantum Phenomena in Condensed Phase Systems

A dissertation presented
by

Emily Rebecca Dunkel

to
The Department of Physics
in partial fulfillment of the requirements
for the degree of
Doctor of Philosophy
in the subject of

Physics

Harvard University
Cambridge, Massachusetts
November 2007

Thesis advisor Author

Subir Sachdev and David Coker **Emily Rebecca Dunkel**

Quantum Phenomena in Condensed Phase Systems

Abstract

This thesis develops mixed quantum-classical methods to model dynamical nonequilibrium quantum phenomena in condensed phase systems, and also explores properties of 2-d systems near a quantum critical point using field theoretic techniques and purely classical simulation.

Mixed quantum-classical methods involve dividing the system into a quantum sub-system coupled to a classical bath, which is useful for examining the dynamics of systems in the condensed phase since the full quantum treatment of a large number of degrees of freedom is often computationally infeasible. Although the bath is treated classically, its coupling to the quantum system precludes a Newtonian description. We implement an approach that uses the quantum-classical Liouville equation to propagate the quantum subsystem density matrix, which results in an ensemble of surface-hopping trajectories. We test this method on model systems and compare with a linearized path-integral approach. We also develop a novel approach to propagating the reduced density matrix that incorporates ideas from both methods while maintaining the ease of implementation of linearized methods.

We study the 2-d spin gap antiferromagnet, piperanzium hexachlorodicuprate (PHCC) near a quantum critical point, where the spin gap is closed by an applied magnetic field, and excitations behave like $S_z = 1$ bosons. Using field theoretic techniques, we find that the temperature dependence of the propagating mode energy is successfully described by a self-consistent Hartree-Fock theory of spin excitations. We also investigate the thermally excited 2-d dilute Bose gas near a quantum critical point, which can be used to obtain the dynamic spectrum of PHCC and other 2-d antiferromagnets. While the pairwise interactions between bosons are weak, we find that the collective properties pose a strong coupling problem (in contrast to the 3-d case). We describe these interactions effectively with a classical model.

Contents

Citations to Previously Published Work

Portions of Chapter 4 will appear in the following paper:

> "Reduced Density Matrix Propagation: An Iterative Scheme for Implementing the Linearized Approach to Nonadiabatic Dynamics in the Mapping Representation (ISLAND-Map)", E. R. Dunkel, S. Bonella, and D. F. Coker

Portions of Chapter 6 will appear in the following paper:

> "Field-induced quantum criticality in a two-dimensional antiferromagnet", T. Hong, E. Dunkel, S. Sachdev, M. Kenzelmann, M. Bouloubasis, M. Stone, C. Broholm, and D. H. Reich.

Chapter 7 has appeared in its entirety in the following paper:

> "Quantum critical dynamics of the two-dimensional Bose gas", S. Sachdev and E. R. Dunkel, Physical Review B **73**, 085116 (2006).

Acknowledgments

I am very grateful to Prof. David Coker for being such a supportive advisor and mentor. His enthusiasm was contagious. I thank Prof. Subir Sachdev for guiding me through my first projects and looking out for me during my time as a graduate student.

Thanks to my collaborators, Dr. Sara Bonella, on quantum-classical methods, and Tao Hong, who performed neutron scattering experiments. Thanks to Prof. Feng Wang and Prof. Tom Castonguay for teaching me about molecular dynamics. Thanks to the Coker group at Boston University for welcoming me into their lab. Thank you Prof. Melissa Franklin and Prof. Markus Greiner for being on my committee.

I am grateful for all my friends in the Physics Department at Harvard who made graduate school fun, especially Lisa. I'd also like to thank my boyfriend, Brian, for all his support.

Dedicated to my mom, Patty
my dad, Darrel
and my brother, Mark

Chapter 1

Introduction and structure of thesis

While quantum interference between macroscopic states is absent in everyday experience, such Schrödinger "cat" states have been observed experimentally, at least transiently. The observation of sustained microsystem coherence despite strong coupling to the environment is a signature of these "cat"-like state. [26] In the limit of zero coupling, a microsystem prepared in a superposition of states will maintain coherence indefinitely. Turning on the coupling leads to energy transfer with the environment. Each microsystem state will launch the bath into a distinct evolution history, and continued coherence of the microsystem implies bath-bath coherence. Whether this is macroscopic or not depends upon the number of bath modes involved.

The system becomes decoherent due to either phase damping or the eventual orthogonality of the bath over time. This is measured by the decay of the off-diagonal elements of the reduced density matrix (obtained by taking the trace of the entire system density matrix over the environmental degrees of freedom). Although measurements are performed on the microstate, inferences about the environment can be made due to the entanglement of the microsystem and bath wavefunctions. [57]

Recent experiments by Apkarian et al [59] have demonstrated “cat”-like states by measuring the vibrational decoherence of impurity molecular iodine coupled to a solid Kr bath using four-wave mixing. They prepare the impurity in a superposition of two vibrational states on the B-electronic state and let the system evolve. The impurity collides with the bath, driving two distinct bath histories. They find that the coherence of the two states persists for approximately nine vibrational periods, and since the impurity is strongly coupled to the bath, the bath itself must also be in a superposition of states during this time. After the nine vibrational periods, there is complete decoherence, corresponding to the transition between quantum dynamics and the classical macroscopic world. The ability to simulate systems like this is of great interest. The large number of degrees of freedom make a full quantum simulation infeasible, and thus we must resort to approximate methods. Mixed quantum-classical methods are one avenue of approach, in which for this problem, the impurity molecular iodine is treated quantum mechanically and the solid Kr environment is treated classically. The development and implementation of mixed quantum-classical methods is the subject of Chapters 2 - 4 of this thesis.

Chapter 2 provides an overview of mixed quantum-classical methods. In Chapter 3 we build upon an approach developed by MacKernan, Ciccotti and Kapral [29] that uses the quantum-classical Liouville equation to propagate the quantum system density matrix, resulting in an ensemble of trajectories that have hops between population and coherences in the representation of the density matrix, or "surface hopping" trajectories. We implement this on model condensed phase systems and compare results with a path-integral approach that is linearized in the forward and backward bath variables, developed and coded previously in the Coker group [7]. In Chapter 4, in collaboration with Dr. Sara Bonella, we develop a novel approach for propagating the quantum system density matrix that incorporates ideas from both methods yet maintains the ease of implementation of linearized methods. The method is based on a time stepping procedure arising from a Trotter factorization, combining the forward and backward incremental propagators, and treating sums over quantum states with a Monte Carlo surface hopping-like procedure. The ability to describe decoherence in Apkarian's experiment on B-state molecular iodine motivated the development of this new method. The linearized approach in the pure dephasing limit has been successfully used to describe X-electronic state dynamics [28]. In the B-state, however, population relaxation must also be included since this state is coupled strongly to the bath. The B-state system is a highly asymmetric problem, which the linearized method has difficulties with as shown in Chapter 3. Branching of nuclear trajectories, which is not included in the linearized approach, may also play an important role in the B-state decoherence. Thus, Chapter 4 is devoted to the development of a more accurate method. These chapters were done under the advising of Prof. David Coker.

Chapters 5 - 7 are devoted to the study of quantum phase transitions, which occur at zero temperature and result from tuning a non-thermal control parameter. In these transitions order is destroyed by quantum fluctuations rooted in the Heisenberg uncertainty principle, as opposed to thermal fluctuations in the classical case. Chapter 5 gives an overview of phase transitions and discusses coupled dimer antiferromagnets and the bond operator approach. While quantum phase transitions are of great interest, it has been difficult to find systems that are both theoretically tractable and can be tuned experimentally across a quantum phase transition. In recent experiments, however, on 2-d insulating spin-gap compounds [40, 58, 79, 68, 67, 22] a transition was accessible by tuning an applied magnetic field. In these systems the low lying spin excitations behave like spin $S_z = 1$ bosons and condensation of these bosons at a critical magnetic field corresponds to a phase transition. We study one of these compounds, piperanzium hexachlorodicuprate (PHCC), in Chapter 6. Using data from neutron scattering experiments by Tao Hong et al [22] we find that the propagating mode energy is successfully described by a self-consistent Hartree-Fock theory of spin excitations. In Chapter 7 we investigate the thermally excited 2-d dilute Bose gas near a quantum critical point. In 3-d the quantum critical fluctuations can be described by the Bose-Einstein theory of non-interacting bosons, but this is not the case in 2-d. While the pairwise interactions between bosons are weak, we find that the collective properties pose a strong coupling problem, which can be described by an effective classical model. This can be applied to obtain the dynamic spectrum of PHCC. These chapters were done under the advising of Prof. Subir Sachdev.

Chapter 2

Quantum dynamics

2.1 Introduction

The dynamics of quantum particles interacting with more massive particles is an active field of study [9], from the vibrational dephasing of an impurity molecule in a lattice discussed in Chapter 1, to proton transfer in solution. The large number of degrees of freedom in condensed phase systems make exact simulation difficult and thus the development of approximate methods is a very active area of research in chemical physics.

2.2 Approximate methods

A variety of approximate methods to simulate large quantum systems have been developed and can be broadly divided into semiclassical, linearization, and mixed quantum-classical approaches.

In semiclassical methods [2, 5, 37, 65, 69], all degrees of freedom are treated on the same footing, while hopefully still capturing the quantum character to a satisfactory extent. The quantum propagator is expressed as a weighted average of classical trajectories determined by a stationary phase analysis of the path-integral representation of the propagator. [19, 35] This becomes exact in the limit that $S/\hbar \rightarrow \infty$, where S is the system's classical action. One advantage of these methods is that the semiclassical propagator can be obtained by classical simulation techniques. The weights, however, are a source of numerical instability since one must handle interference effects between trajectories. In chaotic systems this instability becomes even more pronounced and requires the use of often expensive filtering techniques [25, 31, 75]. Linearized semiclassical initial value representation (LSC-IVR) methods [69, 71, 76] provide another way to handle the oscillatory integrals in semiclassical methods. The correlation function expressed as a double phase space average is expanded to linear order in the difference between phase space variables in the two action integrals. A drawback of this method is that it is incapable of describing quantum coherence effects that arise from distinct classical trajectories [71]. A systematic way of going beyond this is given by the forward-backward initial value representation (FB-IVR) approach [32, 36, 70], in which the forward and backward time evolution is combined into one overall semiclassical initial value representation (SC-IVR) propagation. This partially cancels the oscillatory behavior of the integrals, while maintaining the ability to capture quantum coherence effects.

Linearization techniques are another approach [44, 45, 60, 61, 62]. In these methods, the time correlation function is expressed in the Heisenberg representation and is linearized with respect to the forward and backward propagated variables. This results in a set of classical trajectories with initial conditions sampled from the Wigner transform of the density operator. Calculating the Wigner transform is a difficult problem for anharmonic systems and efficient approximate methods have been developed [44, 61]. The formal result obtained by linearization techniques is equivalent to that obtained by the LSC-IVR approach [60]. While linearized schemes are less accurate than their full semiclassical counterpart, they are simpler to implement and provide a valuable tool for simulating systems in the condensed phase.

In mixed quantum-classical methods, on the other hand, the quantum and classical degrees of freedom are treated in different manners. The system is partitioned into a quantum and classical part on the basis of relative masses or energy scales, and the Hamiltonian is of the form:

$$\hat{H} = \frac{\hat{P}^2}{2M} + \hat{h}_{qm}(R, \hat{p}, \hat{r}) \tag{2.1}$$

where $(\hat{r}, \hat{p})$ describe the quantum subsystem and (R, P) the classical bath. $\hat{h}_{qm}$ is the quantum sub-system Hamiltonian which depends upon the bath positions. Although the bath is treated classically, a simple Newtonian description of its evolution no longer exists due to its coupling to the quantum system. Approaches of this type are the subject of the next two chapters.

The simplest mixed quantum-classical approach assumes adiabatic dynamics. The time independent Schrödinger equation is solved for a fixed bath configuration to obtain the quantum subsystem's eigenstates and adiabatic energies. This is done repeatedly over different bath configurations to map out a potential energy surface as a function of R. The bath molecules are then evolved with Newton's equations subject to the Hellmann-Feynman forces [13] determined from the adiabatic energies. This approach is only valid when the energy difference between states is large and the coupling between the quantum and bath degrees of freedom is small, otherwise motion on a single Born-Oppenheimer surface is no longer valid [72].

Mean field, surface hopping, and quantum-classical linearization methods have been developed to account for the breakdown of non-adiabaticity. In mean field, or Ehrenfest methods, the classical particles move over an interaction potential determined by the average of the quantum subsystem. This approach fails when the mean potential does not provide an accurate picture of the system. In surface hopping methods [17, 18, 46, 63], the classical particles are propagated over one of the potential energy surfaces with stochastic hops between quantum states. These transitions are handled with an *ad hoc* procedure that distributes the trajectories to mimic the population evolution of the quantum subsystem. [9] Surface hopping has proven to be quite successful in describing condensed phase phenomena [4, 78], although retaining quantum coherence is a limitation of these algorithms, and approximate methods have been introduced to include decoherence effects [3, 18].

Methods have also been developed based on various approximations to the Liouville equation which evolves the density matrix for the entire system. A common simple approach in the quantum optics literature [34, 41] for handling system-bath interactions involves integrating the Liouville equation, tracing over the bath variables, and making the Markovian approximation which assumes that the bath-bath correlation decay time is infinitely short. This gives the master equation for the reduced density operator, and expanding in a basis of coherent states leads to the

Fokker-Plank equation. In quantum-classical Liouville methods, on the other hand, the approximation to the Liouville dynamics is made at the beginning. The Liouville equation is expanded on the basis of relative mass or energy scales of the system and bath, to give the quantum-classical Liouville equation. This method does not make the Markovian assumption and can take into account bath coherence effects. It also treats the bath variables explicitly. Taking a phase space representation for the bath variables and integrating the quantum-classical Liouville equation gives the evolution equation for the reduced density matrix. This results in an ensemble of surface hopping trajectories [12, 24, 30]. In between hops the trajectories can run on a coherence of states, thus this approach maintains quantum coherence in a more rigorous way than standard surface hopping or mean field methods. We explore a quantum-classical Liouville approach in detail in Chapter 3.

Linearization methods [6, 7, 8] are another avenue of approach we explore in Chapter 3. Like the semiclassical linearization methods discussed above, the time correlation function is expressed in the Heisenberg representation, but in these methods the linearization is carried out in the bath variables only. Transitions between quantum states are handled by the mapping formalism [35, 65] in which the discrete quantum states are mapped onto continuous degrees of freedom. A limitation of linearized approaches is that they are accurate only in the short time limit. Correlation functions in condensed phase systems decay rapidly, however, enabling linearized approaches to yield reliable results.

2.3 Discussion

In Chapter 3 we build upon the trotterized Wigner-Liouville method developed by D. MacKernan, G. Ciccotti and R. Kapral [29] and implement this for model condensed phase systems. We compare the results with a mixed quantum-classical linearized approach developed and coded previously in the Coker group [7], and find that the Wigner-Liouville method captures the dynamics more accurately at longer times and lower temperatures, and for asymmetric problems. The fundamental physical difference between these two approaches is that nuclear trajectory branching is included only in the Wigner-Liouville method. Disadvantages of this method are that it is much more difficult to implement, and also requires the use of filters which are highly dependent upon system parameters. A disadvantage of the linearized approach is that the trajectories depend upon the measurement, as is shown when we study the coupled Morse oscillator system. The method also produces so-called “ghost” trajectories, or trajectories with approximately zero weight. In Chapter 4, in collaboration with Dr. Sara Bonella, we develop a novel approach that incorporates ideas from both methods yet maintains the ease of implementation of linearized methods. We linearize in the short time limit with stochastic hops between density matrix elements. This approach avoids “ghost” trajectories and forces which depend on the matrix element of the observable. This new approach takes into account nuclear branching and is able to capture bath-bath coherence effects. Both chapters were done under the advising of Professor David Coker.

Chapter 3

Mixed quantum-classical approaches and tests on model systems

3.1 Wigner-Liouville approach

The first approach we implement is based on the Trotter decomposition of the quantum-classical propagator, developed by Dónal Mac Kernan, Giovanni Ciccotti, and Raymond Kapral in Ref. [29], which describes the dynamics of a quantum system coupled to its classical environment. The propagator is divided into small time steps and quantum transitions are Monte Carlo sampled to yield a surface-hopping type approach.

3.1.1 Theory

When investigating the dynamics of quantum systems, one is often interested in the time evolution of the expectation value of some operator, $\hat{A}$. This time evolution is governed by the Heisenberg equation: $i\hbar\partial\hat{A}/\partial t = [\hat{H}, \hat{A}(t)]$, where $\hat{H}$ is the Hamiltonian. Conversely, in classical mechanics, an observable is a function of phase space (R, P), and its evolution is given by: $\partial A/\partial t = \{H, A(t)\}$. We would therefore expect an observable evolved by a mixed quantum-classical approach to have both operator and phase space character, and the evolution equations to involve both commutators and Poison brackets. Starting with a full quantum description and expanding to lowest order in the square root of the quantum to classical mass ratio, $\mu = (m/M)^{\frac{1}{2}}$, gives the quantum-classical Liouville equation [24]:

$$\begin{aligned}\frac{\partial\hat{A}_W}{\partial t} &\approx -\frac{i}{\hbar}[\hat{H}_W, \hat{A}_W] + \frac{1}{2}(\{\hat{H}_W, \hat{A}_W\} - \{\hat{A}_W, \hat{H}_W\}) \\ &\equiv i\hat{\mathcal{L}}\hat{A}_W(t) \qquad (3.1)\end{aligned}$$

where $\hat{\mathcal{L}}$ defines the quantum-classical Liouville operator, and the partial Wigner transform of $\hat{A}$ over the bath variables, (R, P), is given by [72]:

$$\hat{A}_W(R, P) = \int dz e^{iP\cdot z}\langle R - \frac{z}{2}|\hat{A}|R + \frac{z}{2}\rangle \qquad (3.2)$$

Please see Appendix A for details of the derivation. The quantum classical Liouville equation is able to describe the dynamics of systems accurately when $m << M$ [23] or the characteristic energy scale of the quantum subsystem is much higher than that of the bath. Further, for the spin boson model, the linear order expansion is exact, so the quantum classical Liouville dynamics is equivalent to a full quantum description [30]. While the formal solution is simply $\hat{A}_W(t) = exp(i\hat{\mathcal{L}}t)\hat{A}_W(0)$, its simulation is not an easy task.

Formulating the problem in the adiabatic basis is convenient for a surface-hopping scheme. The adiabatic eigenfunctions, $|\alpha, R\rangle$, are solutions of the eigenvalue problem:

$$\hat{h}_W(R)|\alpha, R\rangle = E_\alpha(R)|\alpha, R\rangle \tag{3.3}$$

where $\hat{h}_W(R) = \hat{p}^2/(2m) + \hat{V}_W(\hat{q}, R)$ is the partially Wigner transformed subsystem Hamiltonian for fixed bath coordinates. The full system Hamiltonian is given by $\hat{H}_W = \hat{P}^2/(2M) + \hat{h}_W(R)$. Small variables refer to the quantum system and large variables to the bath, and we will assume *hat* notation where appropriate. Defining the matrix elements of the operator as: $A_W^{\alpha\alpha'}(R, P) = \langle\alpha, R|A_W|\alpha', R\rangle$, the quantum-classical Liouville Equation becomes:

$$\frac{\partial A_W^{\alpha\alpha'}}{\partial t}(R, P, t) = \sum_{\beta\beta'} i\mathcal{L}_{\alpha\alpha'\beta\beta'} A_W^{\beta\beta'}(R, P, t) \tag{3.4}$$

Taking $w_{\alpha\alpha'}(R) = (E_\alpha(R) - E'_\alpha(R))/\hbar$, gives the following expression for the quantum-classical Liouville super-operator that propagates the system [30]:

$$\begin{aligned} -i\mathcal{L}_{\alpha\alpha'\beta\beta'} = \quad & (-iw_{\alpha\alpha'} - iL_{\alpha\alpha'})\delta_{\alpha\beta}\delta_{\alpha'\beta'} + J_{\alpha\alpha'\beta\beta'} \\ & \equiv i\mathcal{L}^0_{\alpha\alpha'}\delta_{\alpha\beta}\delta_{\alpha'\beta'} + J_{\alpha\alpha'\beta\beta'} \end{aligned} \tag{3.5}$$

Where the classical Liouville operator is defined by:

$$iL_{\alpha\alpha'} = \frac{P}{M} \cdot \frac{\partial}{\partial R} + \frac{1}{2}(F_W^{\alpha\alpha} + F_W^{\alpha'\alpha'}) \cdot \frac{\partial}{\partial P} \tag{3.6}$$

and $F_W^{\alpha\alpha} = -\langle\alpha, R|\partial V_W(q, R)/\partial R|\alpha, R\rangle$, which is the Hellmann-Feynman force that governs the motion on the adiabatic surface corresponding to $|\alpha, R\rangle$.

The $J_{\alpha\alpha'\beta\beta'}$ super-operator accounts for non-adiabatic transitions and the resulting momentum transfer to and from the bath:

$$J_{\alpha\alpha'\beta\beta'} = -\frac{P}{M} \cdot d_{\alpha\beta}(1 + \frac{1}{2}S_{\alpha\beta} \cdot \frac{\partial}{\partial P})\delta_{\alpha'\beta'} - \frac{P}{M} \cdot d^*_{\alpha'\beta'}(1 + \frac{1}{2}S^*_{\alpha'\beta'} \cdot \frac{\partial}{\partial P})\delta_{\alpha\beta} \tag{3.7}$$

where $S_{\alpha\beta} = (E_\alpha - E_\beta)d_{\alpha\beta}(\frac{P}{M} \cdot d_{\alpha\beta})^{-1}$ and the coupling matrix element is $d_{\alpha\beta} = \langle\alpha, R|\nabla_R|\beta, R\rangle$.

The evolution operator can be written in a Dyson type form:

$$(e^{-i\mathcal{L}t})_{\alpha\alpha'\beta\beta'} = e^{-i\mathcal{L}^0_{\alpha\alpha'}t}\delta_{\alpha\beta}\delta_{\alpha'\beta'} + \sum_{\gamma\gamma'}\int_0^t dt' e^{-i\mathcal{L}^0_{\alpha\alpha'}(t-t')} J_{\alpha\alpha'\gamma\gamma'}(e^{-i\mathcal{L}t'})^{\gamma\gamma'\beta\beta'} \tag{3.8}$$

and can be iterated in powers of the perturbation J.

Trotter factorizing into N steps of interval $\delta = t/N$, and using the fact that $\mathcal{L}^0$ is diagonal in the adiabatic basis, gives the short time propagator [30]:

$$(e^{i\mathcal{L}\delta})_{\alpha\alpha'\beta\beta'} \approx (e^{i\mathcal{L}^0\delta/2})_{\alpha\alpha'\alpha\alpha'}(e^{-J\delta})_{\alpha\alpha\beta\beta'}(e^{i\mathcal{L}^0\delta/2})_{\beta\beta'\beta\beta'} + \mathcal{O}(\delta^3) \tag{3.9}$$

So, we see that the full propagator consists of free propagation with intermittent hops between "surfaces". These surfaces do not correspond to a single adiabatic surface in the usual sense in surface hopping methods [17, 18, 46, 63], but instead consists of two adiabatic surfaces (for the bra and ket states). Hops take place between populations and coherences in the representation of the quantum subsystem density matrix.

The expectation value of an observable is given by:

$$\langle A(t)\rangle = Tr' \int dRdPe^{i\mathcal{L}t}A_W(R, P, 0)\rho_W(R, P, 0) \tag{3.10}$$

where Tr' is the trace over the quantum subsystem. Solutions can be represented in terms of an ensemble of surface-hopping trajectories sampled from the initial density and propagated by the Liouville super-operator.

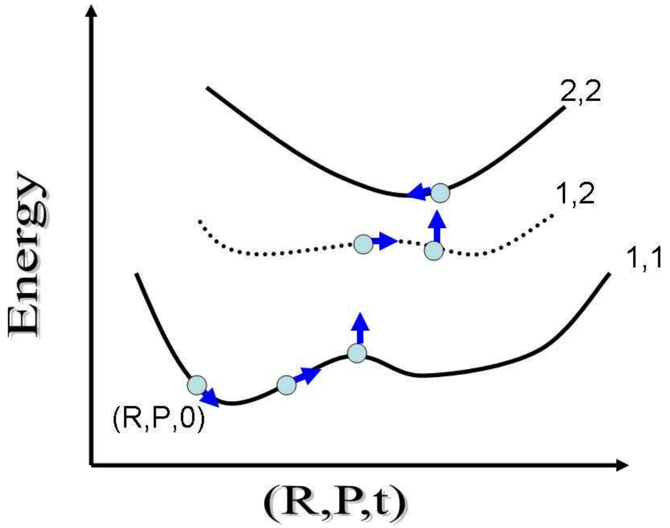

Figure 3.1: A trajectory starts on state $(1,1)$ and is propagated by L_{11}. A transition to state $(1,2)$ occurs due to the perturbation J and a quantum coherence is created. Propagation continues by L_{12}, followed by a transition to state $(2,2)$.

3.1.2 Implementation and discussion

Here we make some comments about the procedure, with details given in Appendix B.

Figure 3.1 gives an example of a single trajectory. This trajectory starts on the ground potential energy surface, and is propagated by the classical Liouville operator, L_{11}. The observable during this time is diagonal, A^{11}. A nonadiabatic transition from state $(1,1)$ to state $(1,2)$ occurs stochastically due to the J perturbation. The energy gap and coupling vectors restrict the nature of these hops (please see Appendix B for more detail). The transition is accompanied by a change in the bath momenta in such a way as to conserve the total energy of the system. The system is now in a coherent state, and the observable is given by the off-diagonal matrix element, A^{12}. The trajectory is propagated by L_{12} and accumulates a phase factor given by the time integral of w_{12}. A second stochastic transition occurs, this time from state $(1,2)$ to state $(2,2)$, and the observable during this time is diagonal, A^{22}. The final observable, A, is constructed from an ensemble of trajectories, with stochastic quantum transitions.

One of the approximations made in the algorithm was dividing the propagator into small time steps and trotter factorizing into terms involving $\mathcal{L}^0$ and J. This introduces an error of $\mathcal{O}(\delta^3)$. Secondly, a jump approximation was made, valid to $\mathcal{O}(\delta^2)$. Branching of each trajectory into three trajectories occurs with each application of $exp(-J\delta)$, that is $(R,P) \rightarrow (R,P)$ or $(R,P-\delta P)$ or $(R,P+\delta P)$, and leads to exponential growth in the number of trajectories. This branching was eliminated by taking a small time step expansion yielding an energy conserving single trajectory. A limitation of this is that it does not allow for the possibility of tunneling.

We represent our adiabatic energy surfaces for two state systems using mixing angles to avoid numerical instabilities, discussed in Appendix B (for an arbitrary number of states, the eigenvectors would need to be solved numerically). Finally, filters were used to limit the maximum number of hops and maximum value of the observable, which fluctuates largely when the hopping probability is high (please see Appendix B for more detail). These fluctuations exacerbate the sign problem that comes from the evolution phase factors and makes it difficult to obtain accurate Monte Carlo estimates. A filter is therefore used to eliminate these fluctuations that should not contribute to the average.

In summary, the equations of motion are obtained by taking a Wigner transform over the bath degrees of freedom of the Liouville equation, which describes the full quantum system, and expanding in the mass ratio of the quantum to classical particles. The series solution of the resulting quantum-classical Liouville equation leads to an ensemble of surface hopping trajectories, where hops between quantum states are selected stochastically. This method is different from traditional surface-hopping schemes in that it contains segments of coherent evolution, as opposed to simply moving on a single adiabatic surface between quantum transitions.

3.2 Linearized quantum-classical method

This section outlines the linearized approach developed and coded previously in the Coker group [6, 7, 8]. It involves partial linearization of the full quantum path-integral expression for the time correlation function, and uses the mapping formalism in which the discrete quantum states are represented in terms of continuous harmonic oscillator degrees of freedom.

3.2.1 Theory

The correlation function of two operators in the Heisenberg representation is given by:

$$\langle \hat{A}\hat{B}(t)\rangle = Tr[\hat{\rho}\hat{A}e^{i\hat{H}t}\hat{B}e^{-i\hat{H}t}] \tag{3.11}$$

$\hat{H}$ is the full system Hamiltonian: $\hat{H} = \hat{P}^2/(2M) + \hat{h}_{qm}(R)$, where $\hat{h}_{qm}$ is the quantum subsystem Hamiltonian and (R, P) refer to the bath variables. $\hat{\rho}$ is the initial system density operator. We work in units where $\hbar = 1$ and will assume *hat* notation where appropriate.

The correlation function can be written in a basis set, $|R, \alpha\rangle = |R\rangle|\alpha\rangle$, chosen as the tensor product of the bath degrees of freedom and the diabatic electronic basis (the diabatic representation is used since the evolution equations obtained are much simpler than in the adiabatic basis [9]). Inserting resolutions of the identity into Eq. (3.11) gives:

$$\begin{aligned}\langle AB(t)\rangle = \quad & \sum_{\alpha\beta\alpha'\beta'} \int dR_0 dR_N d\tilde{R}_0 \langle R_0\alpha|\rho A|\tilde{R}_0\alpha'\rangle \\ & \times\langle \tilde{R}_0\alpha'|e^{iHt}|R_N\beta'\rangle\langle \tilde{R_N}\beta'|B|R_N\beta\rangle\langle R_N\beta|e^{-iHt}|R_0\alpha\rangle \qquad (3.12)\end{aligned}$$

This can be read as propagation of the initial state, $|R_0\alpha\rangle$, forward in time followed by a B measurement that may put the system in a different bath or quantum state. The evolution then continues backward in time. The trace is completed by evaluating the corresponding matrix element of A with the density operator. This is shown in Figure 3.2. Note that transitions between quantum states can occur during the evolution.

The n diabatic states are represented using the mapping formalism [33, 37, 64, 66] where they are mapped onto n oscillators:

$$|\alpha\rangle \rightarrow |m_\alpha\rangle = |0_1, ..., 1_\alpha, ..0_n\rangle \qquad (3.13)$$

where there is at most one quantum of excitation in a specific oscillator. The discrete quantum states are thus represented by continuous mapping variables given by classical harmonic oscillator position and momentum of the forward and backward states, (q_α, p_α) and $(\tilde{q}_{\alpha'}, \tilde{p}_{\alpha'})$.

The quantum subsystem Hamiltonian, h_{qm}, is replaced with the mapping Hamil-

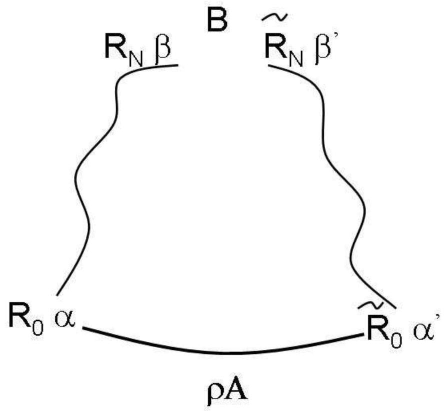

Figure 3.2: Path structure for measurement of the correlation function. $|R_0, \alpha\rangle$ is propagated forward in time and $|\tilde{R}_0, \alpha'\rangle$ is propagated backward in time, and are connected by a B measurement.

tonian:

$$h_m(R) = \frac{1}{2}\sum_{\eta} h_{\eta,\eta}(R)(q_\eta^2 + p_\eta^2 - \hbar) + \frac{1}{2}\sum_{\eta,\eta'} h_{\eta,\eta'}(R)(q_{\eta'}q_\eta + p_{\eta'}p_\eta) \tag{3.14}$$

where $h_{\eta,\eta'} = \langle\eta|h_{qm}|\eta'\rangle$. The forward and backward mapping variables can be evolved independently with Hamilton's equations. For a more detailed development of the mapping formulation in a slightly different context we direct the reader to Section 4.3.2 below.

The kinetic and potential terms of the propagator are trotter factorized, and the bath degrees of freedom are represented in path integral form. The mapping variables are represented in terms of coherent states, and integrals involving the mapping variables are sampled with focused initial conditions obtained by a steepest descent analysis [6]. For details, please see Reference [7].

A change of variables in the bath degrees of freedom is performed:

$$\begin{aligned}\bar{R}_k &= \frac{R_k + \tilde{R}_k}{2} \\ \Delta R_k &= R_k - \tilde{R}_k\end{aligned}$$

and likewise in P, so the bath paths now appearing in the calculation are the mean and difference of the original forward and backward paths. Expanding to linear order in ΔR leads to the final expression for the correlation function:

$$\begin{aligned}\langle AB(t)\rangle \sim & \sum_{\alpha\beta,\alpha'\beta'} \int d\bar{R}_0 dq_0 dp_0 d\tilde{q}_0 d\tilde{p}_0 \int \prod_{k=1}^{N} d\bar{R}_k \frac{d\bar{P}_k}{2\pi\hbar} (\rho A)_W^{\alpha,\alpha'}(\bar{R}_0, \bar{P}_1) \\ & \times (B)_W^{\beta',\beta}(\bar{R}_N, \bar{P}_N) r_{0\alpha} e^{i\theta_{0,\alpha}} \tilde{r}_{0\alpha'} e^{-i\tilde{\theta}_{0,\alpha'}} \\ & \times r_{t,\beta}(\{\bar{R}_k\}) \tilde{r}_{t,\beta'}(\{\bar{R}_k\}) e^{-i\epsilon \sum_{k=1}^{N}(\theta_\beta(\bar{R}_k) - \tilde{\theta}_{\beta'}(\bar{R}_k))} \\ & \times \prod_{k=1}^{N-1} \delta\left(\frac{\bar{P}_{k+1} - \bar{P}_k}{\epsilon} - F_k^{\beta,\beta'}\right) \prod_{k=1}^{N} \delta\left(\frac{\bar{P}_k}{M} - \frac{\bar{R}_k - \bar{R}_{k-1}}{\epsilon}\right)\end{aligned} \qquad (3.15)$$

where we have left out some constants. r and θ describe the mapping variables in polar representation. The force is given by:

$$\begin{aligned}F_k^{\beta,\beta'} &= -\frac{1}{2}\left\{\nabla_{\bar{R}_k} h_{\beta,\beta}(\bar{R}_k) + \nabla_{\bar{R}_k} h_{\beta',\beta'}(\bar{R}_k)\right\} \\ & -\frac{1}{2}\sum_{\lambda\neq\beta} \nabla_{\bar{R}_k} h_{\beta,\lambda}(\bar{R}_k) \left\{\frac{(p_{\beta k} p_{\lambda k} + q_{\beta k} q_{\lambda k})}{(p_{\beta k}^2 + q_{\beta k}^2)}\right\} \\ & -\frac{1}{2}\sum_{\lambda\neq\beta'} \nabla_{\bar{R}_k} h_{\beta',\lambda}(\bar{R}_k) \left\{\frac{(\tilde{p}_{\beta' k} \tilde{p}_{\lambda k} + \tilde{q}_{\beta' k} \tilde{q}_{\lambda k})}{(\tilde{p}_{\beta' k}^2 + \tilde{q}_{\beta' k}^2)}\right\}\end{aligned} \qquad (3.16)$$

We see that the delta functions cause the mean bath particles to follow a simple classical evolution, albeit with complicated forces. These forces are determined by the gradient of the quantum system potential energy, as well as the mapping variables. The forces also depend upon the matrix element of the observable, which can be seen from the force labels in Eq. (3.15). These superscripts are identical to the superscripts

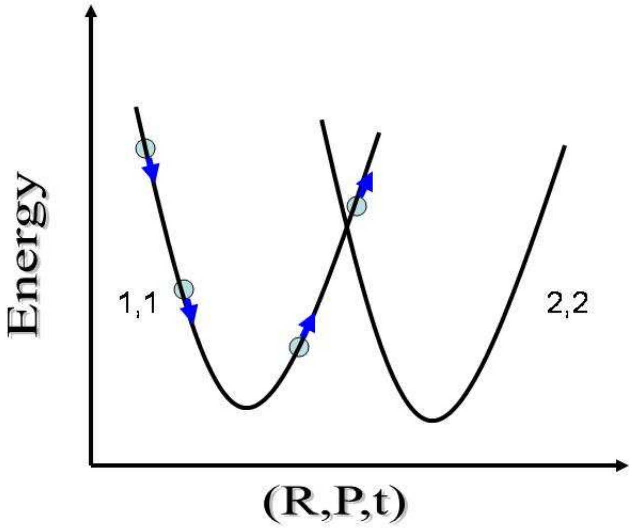

Figure 3.3: The correlation function is obtained by summing over contributions from trajectories representing different matrix elements of the observable, as can be seen from Eq. (3.16). This picture shows a sample trajectory for a system where the off diagonal Hamiltonian matrix elements are independent of R, and the measurement made is of the form B_{11}. In this case, the forces felt by the nuclear trajectory come only from h_{11}, A measurement that is non-diagonal,B_{12} for example, will have forces determined by both surface 1 and 2, as well as the forward and backward mapping variables.

on the Wigner transform of the B measurement. A measurement of the form B^{11}, for example, will involve forces on surface h_{11} and possibly h_{12}, but not h_{22} as can be seen from Eq. (3.16). See Figure 3.3 for a sample trajectory. Bath-bath coherence effects are not included in this approach since a single initial bath condition gives rise to a single trajectory. This method also produces "ghost" trajectories, or trajectories of approximately zero weight, since quantum labels are summed over without taking into account the r amplitude. The evolution of the mapping variables are obtained from Hamilton's equations which depend upon the position of the bath, and thus we see that the evolution of the bath and quantum system are coupled.

3.2.2 Discussion

The linearization in this mixed quantum classical approach was carried out in the bath variables only and thus differs from linearization techniques proposed by a number of authors [44, 60, 62], which linearize in all variables. This full linearization leads to a set of classical trajectories with initial conditions sampled from the Wigner transform of the density operator, and is equivalent to that obtained by the linearized LSC-IVR [60, 69, 71, 76] approach, which uses the semiclassical propagator. A drawback of these method is that they are incapable of describing quantum coherence effects arising from distinct classical trajectories [71]. The forward-backward initial value representation (FB-IVR) semiclassical approach [32, 36, 70], on the other hand, has the ability to capture these quantum coherence effects by combining the forward and backward time evolution into one overall semiclassical initial value representation (SC-IVR) propagation. This method is more difficult to implement than the other linearized approaches.

In summary, the linearized approach we explored involves linearizing in the difference between forward and backward bath paths, and leads to classical evolution of the bath particles. The quantum system was represented by fictitious harmonic degrees of freedom evolved with Hamilton's equations. Unlike semiclassical approaches, the system is no longer described by a single Hamiltonian, but by coupled sets of classical Hamiltonians.

3.3 Tests on model systems

3.3.1 Spin-boson Hamiltonian

The spin-boson model [27, 77] is one of the most popular for testing simulation methods of many-body quantum dynamics since exact results are available [73]. It describes the dynamics of a two level system, with states $|\uparrow\rangle$ and $|\downarrow\rangle$, bilinearly coupled to its environment. This is a simple model for which we can measure quantum coherence and dissipation to the environment. The bath is represented by a set of N harmonic oscillators with masses M_j and frequencies ω_j. A popular choice for the spectral density is Ohmic:

$$J(\omega) = \xi \omega e^{-\omega/\omega_c} \tag{3.17}$$

In dimensionless variables [30], the spin-boson Hamiltonian can be written as:

$$H = -\Omega\sigma_x + \sum_{j=1}^{N} \left[\frac{P_j^2}{2} + \frac{1}{2}\omega_j^2 R_j^2 - c_j R_j \hat{\sigma}_z \right] \tag{3.18}$$

where σ_z and σ_x are the Pauli spin matrices and 2Ω is the energy gap between levels in the bare system. We work in units where $\hbar = 1$ and all frequencies have been scaled by the cutoff frequency, ω_c. In reduced units, the strength of the system-bath coupling is:

$$c_j = \omega_j \sqrt{\xi \omega_0} \tag{3.19}$$

The observable we calculate is the time dependent average population difference, $\langle \sigma_z(t) \rangle$. We assume that the bath and subsystem are initially uncorrelated, and take the subsystem to be in state $|\uparrow\rangle$ and the bath in thermal equilibrium. The initial

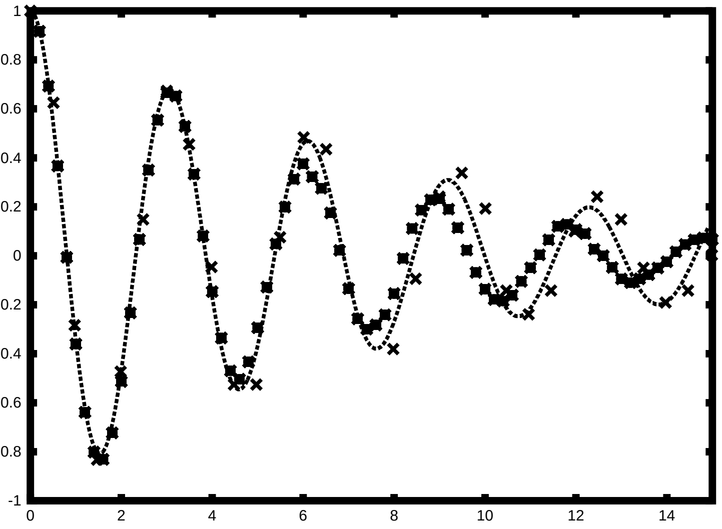

Figure 3.4: $\langle\sigma_z(t)\rangle$vs. Ωt for spin boson model, with parameters: $\Omega = 0.4$, $\xi = 0.09$, $1/T = 12.5$. (x):Exact, (-):Linearized Approach, (*):Wigner-Liouville with jump approximation.

system density matrix is thus:

$$\rho_{sb} = \rho(\mathbf{R}_0, \mathbf{P}_0)| \uparrow\rangle\langle\uparrow | \tag{3.20}$$

where the Wigner transformed bath density is given by:

$$\rho_W(\mathbf{R}_0, \mathbf{P}_0) = \prod_{j=1}^{N} \frac{\tanh(\beta\omega_j/2)}{\pi} e^{-\frac{\tanh\left(\beta\omega_j/2\right)}{\omega_j}\left(\frac{P_{j0}^2}{2}+\frac{\omega_j^2 R_{j0}^2}{2}\right)} \tag{3.21}$$

The system will experience a range of behaviors from coherent oscillation with a period determined by the energy gap, to overdamped relaxation. The behavior depends on the temperature and value of the Kondo parameter, ξ, which determines the strength of the system-bath coupling. We present results for a range of parameters, using both the Wigner-Liouville and linearized method.

Both approaches do quite well compared to exact results. We would expect the linearized approach to be most reliable at higher temperatures, where the density is

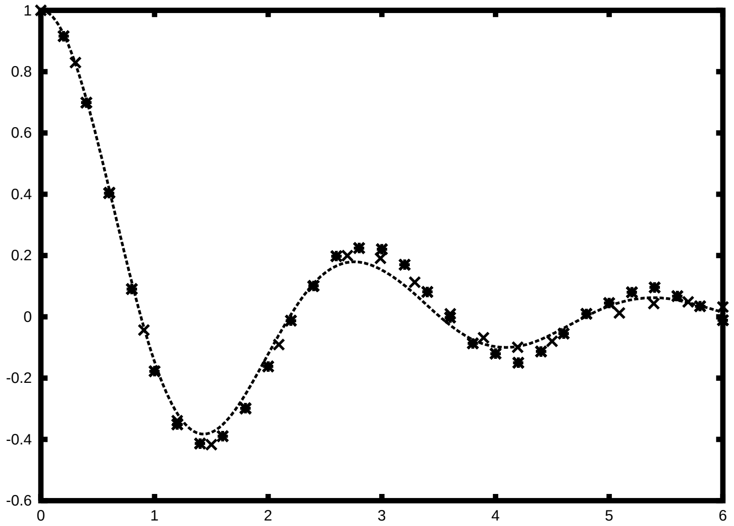

Figure 3.5: $\langle\sigma_z(t)\rangle$ vs. Ωt for spin boson model, with parameters: $\Omega = 0.4$, $\xi = 0.13$, $1/T = 1.0$. (x):Exact, (-):Linearized Approach, (*):Wigner-Liouville with jump approximation.

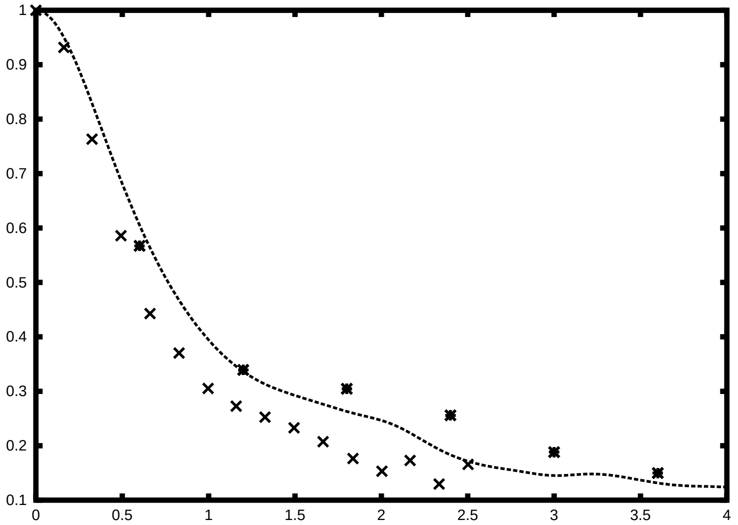

Figure 3.6: $\langle\sigma_z(t)\rangle$ vs. Ωt for spin boson model, with parameters: $\Omega = 1.2$, $\xi = 2.0$, $1/T = 0.25$. (x):Exact, (-):Linearized Approach, (*):Wigner-Liouville with jump approximation.

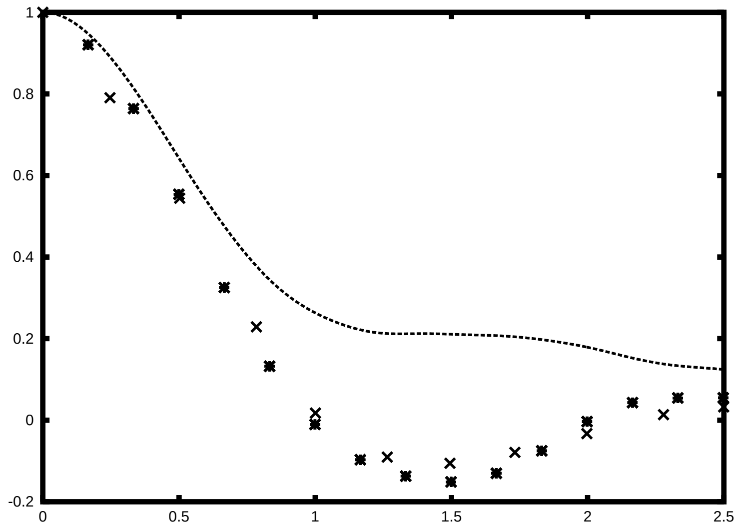

Figure 3.7: $\langle \sigma_z(t) \rangle$ vs. Ωt for spin boson model, with parameters: $\Omega = 0.333$, $\xi = 0.5$, $1/T = 3.0$. (x):Exact, (-):Linearized Approach, (*):Wigner-Liouville with jump approximation.

dominated by diagonal terms and thus the linearization in forward and backwards paths is more reasonable. Also, the linearized method becomes exact in the limit of vanishing friction. We see in Figure 3.7 that at high friction and intermediate temperature, the linearized approach has started to break down. This approach also breaks down for longer times since the differences between forward and backward paths grow.

The Wigner-Liouville approach gives more consistent results than the linearized approach for the range of parameters we probed. For the spin-boson problem, the Quantum-Classical Liouville equation is in fact exact [30] so the error comes from the simulation scheme as opposed to the assumptions that underlie the method. The trotter and jump approximations, and Monte Carlo sampling contribute to the error. Like the linearized approach, the reliability decreases at longer times.

A large advantage the linearized approach has over the Wigner-Liouville approach is that the algorithm is much simpler to implement. It also does not require the use of filters and requires at least an order of magnitude fewer trajectories to converge; for these problems it required around 500 trajectories as opposed to 10^4 for the Wigner-Liouville method. In the rest of this chapter we will look at other model systems to test the reliability of these methods.

3.3.2 Asymmetric spin-boson

In this section, we look at the asymmetric spin-boson model:

$$H = -\Omega\sigma_x + \sum_{j=1}^{N}\left[\frac{P_j^2}{2} + \frac{1}{2}\omega_j^2 R_j^2 - \omega_j\sqrt{\xi\omega_0}R_j\sigma_z\right] + \frac{\Omega}{2}\sigma_z \tag{3.22}$$

in which the minima of the two wells have an energy difference, Ω.

We calculate the average population difference, $\langle\sigma_z(t)\rangle$, and start the quantum subsystem in the higher energy state, $|\uparrow\rangle$, and the bath in thermal equilibrium.

For the system studied in Figure 3.8, the equilibrium value of $\langle\sigma_z\rangle$ should be negative. We see that while the population difference obtained with the Wigner-Liouville method approaches a negative value, the linearized approach gives equal population in both states.

The linearized approach will in fact always give equal population at long times for the asymmetric spin-boson model, due to the nature of the trajectories in this approach. The trajectories depend upon the measurement being made, as can be seen from Eq. (3.16), in which the contributing force matrix elements are determined by the nature of the observable. In the spin-boson problem, the off-diagonal terms in the Hamiltonian are independent of R, and thus for diagonal measurements (such as the population difference), the trajectories will run entirely on either surface one or

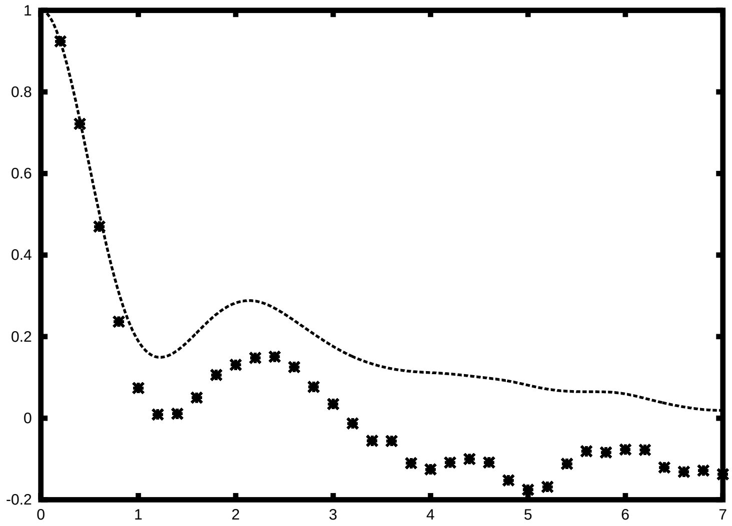

Figure 3.8: $\langle \sigma_z(t) \rangle$ vs. Ωt for asymmetric spin-boson model with parameters: $\Omega = 0.4$, $\xi = 0.13$, $1/T = 1.0$. The statistical limit equilibrium value is: $\langle \sigma_z \rangle = -0.36$. (-):Linearized Approach, (*):Wigner-Liouville with jump approximation.

two, and the population of the two surfaces at long times will be independent of the energy difference. This is a limitation of the linearized approach, which we overcome in Chapter 4 by incorporating hopping between density matrix elements.

3.3.3 Morse Potential

This last problem we consider is meant to model the situation following molecular photo-excitation, which involves non-adiabatic electronic relaxation coupled to nuclear vibrational dynamics. Our model consists of two diabatic Morse oscillator electronic surfaces with Gaussian coupling centered at the crossing bond length. The potential is shown in Figure 3.9.

The electronic Hamiltonian matrix elements are given by:

$$H^{el}_{kk}(R) \quad = \quad D_k(1 - e^{-a_k(R-b_k)})^2 + E_k$$

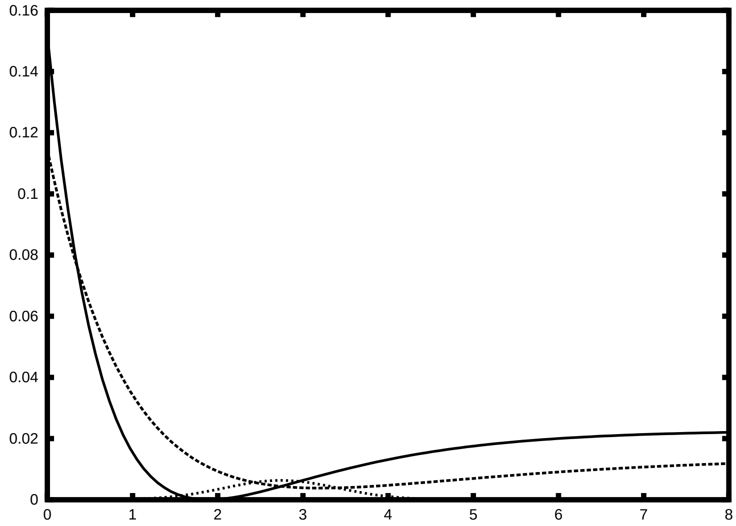

Figure 3.9: This figure shows the diabatic Hamiltonian matrix elements. The left Morse potential is H_{11} and the shallower right Morse potential is H_{22}. The Gaussian centered at the crossing bond length of the two surfaces is H_{12}

$$H_{12}^{el}(R) \quad = \quad A e^{-c(R-R_x)^2} \tag{3.23}$$

where $k = 1, 2$. Working in atomic units, the parameters for surface 1 are: $D_1 = 2.278E-2$, $a_1 = 0.675$, $b_1 = 1.890$, $E_1 = 0$, and surface 2 is given by: $D_2 = 1.025E-2$, $a_2 = 0.453$, $b_2 = 3.212$, $E_2 = 3.8E-3$. Coupling parameters are: $A = 6.337E-3$, $c = 1.12$, $R_x = 2.744$. The initial nuclear configuration involves a Gaussian wavepacket of the form:

$$\chi_1(R, t=0) = \left(\frac{2\alpha}{\pi}\right)^{1/4} e^{-\alpha(R-R_0)^2 - \frac{i}{\hbar}P_0(R-R_0)} \tag{3.24}$$

with $\alpha = 5$, $R_0 = 6$, $P_0 = -5$ that is excited high on the left hand Morse well (surface 1). Surface 2 is initially unpopulated.

This system is challenging because the diabats are anharmonic, and nonadiabatic effects are significant since the wave packet travels back and forth through the coupling region.

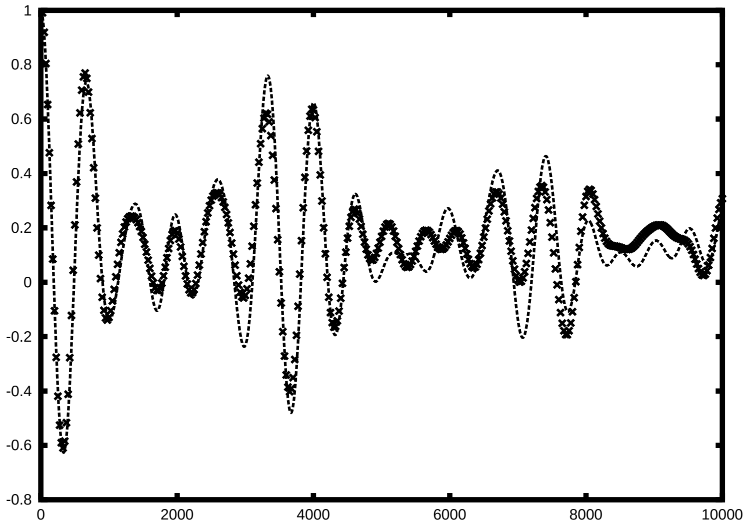

Figure 3.10: $Re(\langle R(0)\sigma_x(0)R(t)\sigma_x(t)\rangle)$ vs. t in atomic units, for the two coupled diabatic Morse surfaces. (x):Exact, (-):Linearized Approach.

In Figure 3.10, we show the real part of $\langle R(0)\sigma_x(0)R(t)\sigma_x(t)\rangle$ as a function of time, calculated with the linearized approach. This correlation function involves off-diagonal electronic operators as well as the nuclear position operator. The high-frequency oscillations are due to the coherent electronic dynamics, while the low frequency modulation is from the nuclear motion. We see that the linearized approach provides reliable results for about two nuclear periods.

In Figure 3.11, we show $\langle \sigma_z(t)\rangle$ as a function of time calculated with the linearized method and see that the behavior is captured only for very short times. It is surprising that this approach works well for the previous correlation function and so poorly for this one. This is due to the fact that the trajectories depend on the observable, as discussed previously.

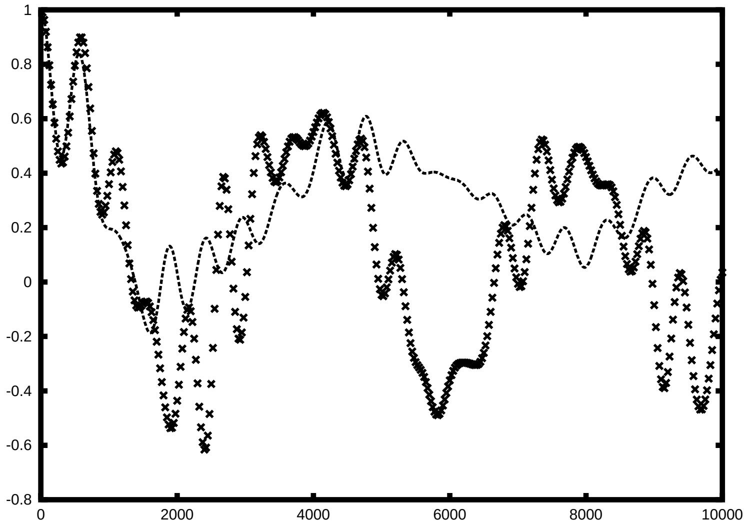

Figure 3.11: $\langle \sigma_z(t) \rangle$ vs. t for the two coupled diabatic Morse surfaces. (x):Exact, (-):Linearized Approach

3.4 Summary

Both approaches provide reliable results for the symmetric spin-boson model, which describes a two level system coupled to a harmonic environment. For the asymmetric spin-boson model, the Wigner-Liouville approach implemented with the jump approximation gives an average population that goes to the correct well, while the linearized approach will always produce equal state population at long times. The reliability of the linearized approach depends on the matrix element of the observable, as shown with the diabatic Morse surfaces.

An advantage of the linearized approach is that it much simpler to implement than the Wigner-Liouville surface hopping method. It also requires at least an order of magnitude fewer trajectories to converge, and does not require the use of filters. The linearized approach, however, is unable to capture bath coherence effects as it does not include nuclear trajectory branching.

In the next chapter, we develop a novel approach for propagating the reduced density matrix, that combines ideas from both methods to remedy some of the shortcomings of the linearized approach while maintaining its ease of implementation.

Chapter 4

Density matrix propagation: an iterative linearized approach

4.1 Introduction

This chapter presents a new approach to propagating the reduced density matrix based on a time stepping procedure arising from a Trotter factorization and combining the forward and backward incremental propagators. The sums over intermediate states of the discrete quantum subsystem are implemented by a Monte Carlo surface hopping-like procedure, while the integrals over the continuous variables are performed using a linearization in the difference between the forward and backward paths of these variables leading to classical-like equations of motion with different forces determined by the quantum subsystem state hopping.

4.2 Theory

The basic approach we develop here involves applying strings of short time propagators on the right and left of some initial density operator to advance it in time. For example, advancing the initial density operator $\hat{\rho}(0)$ of the full system by two steps, each of duration ϵ, is accomplished as follows:

$$\hat{\rho}(2\epsilon) = e^{-\frac{i}{\hbar}\hat{H}\epsilon} e^{-\frac{i}{\hbar}\hat{H}\epsilon} \hat{\rho}(0) e^{\frac{i}{\hbar}\hat{H}\epsilon} e^{\frac{i}{\hbar}\hat{H}\epsilon} \tag{4.1}$$

We suppose the full system Hamiltonian can be conveniently represented in terms of some continuous variables, (R,P), and some discrete quantum states labeled n, so that:

$$\hat{H} = \hat{P}^2/2M + \sum_n \sum_m |n\rangle h_{nm}(R) \langle m| \tag{4.2}$$

where we work in the diabatic basis, given by $|Rn\rangle = |R\rangle|n\rangle$. Inserting resolutions of the identity written as $\int dR_0 \sum_{n_0} |R_0 n_0\rangle\langle R_0 n_0| = \hat{1}$ between each of the operators in Eq. (4.1), labeling states according to time increasing as we move outward from $\hat{\rho}(0)$, and using unprimed labels for propagating forward and primed for propagating backward, we obtain:

$$\begin{aligned} \langle R_2 n_2|\hat{\rho}(2\epsilon)|R_2' n_2'\rangle &= \int dR_1 \sum_{n_1} \int dR_0 \sum_{n_0} \int dR_1' \sum_{n_1'} \int dR_0' \sum_{n_0'} \\ &\times \langle R_2 n_2|e^{-\frac{i}{\hbar}\hat{H}\epsilon}|R_1 n_1\rangle \langle R_1 n_1|e^{-\frac{i}{\hbar}\hat{H}\epsilon}|R_0 n_0\rangle \langle R_0 n_0|\hat{\rho}(0)|R_0' n_0'\rangle \\ &\times \langle R_0' n_0'|e^{\frac{i}{\hbar}\hat{H}\epsilon}|R_1' n_1'\rangle \langle R_1' n_1'|e^{\frac{i}{\hbar}\hat{H}\epsilon}|R_2' n_2'\rangle \end{aligned} \tag{4.3}$$

Each matrix element can be represented in terms of path integrals, and a diagramatic realization of this evolution in terms of these paths is displayed in Fig. 4.1.

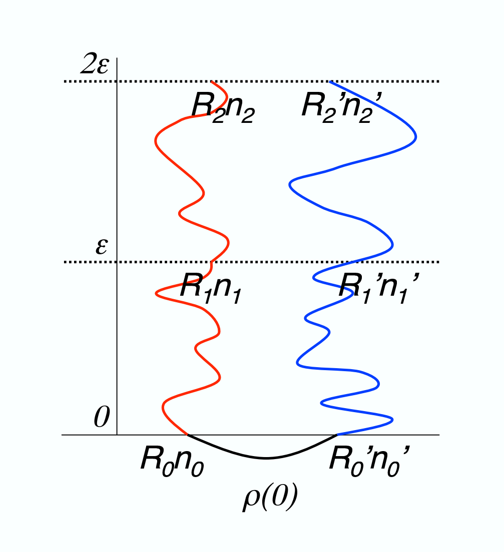

Figure 4.1: Diagramatic representation of the reduced density matrix propagation for two time steps.

Using a hybrid momentum-coordinate representation for the bath variables, we can approximate the short time incremental propagator matrix elements as follows [44]:

$$\lim_{\epsilon\to\infty}\langle R_1 n_1|e^{-\frac{i}{\hbar}\hat{H}\epsilon}|R_0 n_0\rangle = \int \frac{dP_1}{(2\pi\hbar)^d} e^{-\frac{i}{\hbar}\epsilon P_1^2/2M} e^{\frac{i}{\hbar}P_1(R_1-R_0)} \langle n_1|e^{-\frac{i}{\hbar}\hat{h}(R_0)\epsilon}|n_0\rangle \qquad (4.4)$$

where a complete set of eigenstates of $\hat{P}$ has been introduced to evaluate the short time kinetic part of the propagator, and we have used the fact that h_{nm} is diagonal in the bath coordinate representation. A similar expression in primed variables for the backward propagators is obtained. The vectors describing the continuous "nuclear" variables here are d-dimensional.

Using the above short time approximate propagator and transforming to mean and difference path variables defined as

$$\bar{R}_i \;=\; (R_i + R_i')/2$$

$$\Delta R_i = (R_i - R_i')$$

with similar expressions for the $\bar{P}_i$ and ΔP_i variables, and after some straightforward manipulations, we can readily rewrite the time stepping expression in Eq. (4.3) as follows:

$$\begin{aligned}
&\langle \bar{R}_2 + \frac{\Delta R_2}{2} n_2 | \hat{\rho}(2\epsilon) | \bar{R}_2 - \frac{\Delta R_2}{2} n_2' \rangle = (2\pi\hbar)^{2d} \int d\bar{P}_2 \int d\bar{R}_1 \int d\bar{P}_1 \int d\bar{R}_0 \sum_{n_1} \sum_{n_1'} \\
&\times e^{\frac{i}{\hbar}\bar{P}_2 \Delta R_2} \delta(\bar{P}_2 \epsilon / M - (\bar{R}_2 - \bar{R}_1)) F_{n_2, n_2', n_1, n_1'}(\bar{P}_2, \bar{R}_1, \bar{P}_1, \epsilon) \\
&\times \delta(\bar{P}_1 \epsilon / M - (\bar{R}_1 - \bar{R}_0)) \rho^W_{n_1 n_1'}(\bar{R}_0, \bar{P}_1) \qquad (4.5)
\end{aligned}$$

In the above expression we have defined the following quantity:

$$\begin{aligned}
\rho^W_{n_1, n_1', n_0, n_0'}(\bar{R}_0, \bar{P}_1) &= \int d\Delta R_0 \langle \bar{R}_0 + \frac{\Delta R_0}{2} n_0 | \hat{\rho}(0) | \bar{R}_0 - \frac{\Delta R_0}{2} n_0' \rangle e^{-\frac{i}{\hbar}\bar{P}_1 \Delta R_0} \\
&\quad \times \langle n_0' | e^{\frac{i}{\hbar}\hat{h}(\bar{R}_0 - \Delta R_0/2)\epsilon} | n_1' \rangle \langle n_1 | e^{-\frac{i}{\hbar}\hat{h}(\bar{R}_0 + \Delta R_0/2)\epsilon} | n_0 \rangle \qquad (4.6) \\
&= \rho^W_{n_0 n_0'}(\bar{R}_0, \bar{P}_1) \delta_{n_0' n_1'} \delta_{n_1 n_0}
\end{aligned}$$

In the limit of $\epsilon \longrightarrow 0$ the propagators in the matrix elements of the second line in the above expression become unit operators, so the matrix elements become Kronecker δ's in the state labels and $\rho^W_{n_0 n_0'}(\bar{R}_0, \bar{P}_1)$ is the Wigner transform of the reduced density matrix. These δ's are used to kill the initial state sums in Eq. (4.3) and arrive at the expression in Eq. (4.5).

Integrals over ΔP have been performed using:

$$\int d\Delta P_1 e^{-\frac{i}{\hbar}[\bar{P}_1 \epsilon / M - (\bar{R}_1 - \bar{R}_0)]\Delta P_1} = (2\pi\hbar)^d \delta(\bar{P}_1 \epsilon / M - (\bar{R}_1 - \bar{R}_0)) \qquad (4.7)$$

and we have defined the function $F_{n_2, n_2', n_1, n_1'}$ as follows:

$$\begin{aligned}
F_{n_2, n_2', n_1, n_1'}(\bar{P}_2, \bar{R}_1, \bar{P}_1, \epsilon) &= \int d\Delta R_1 \langle n_2 | e^{-\frac{i}{\hbar}\hat{h}(\bar{R}_1 + \Delta R_1/2)\epsilon} | n_1 \rangle \\
&\quad \times \langle n_1' | e^{\frac{i}{\hbar}\hat{h}(\bar{R}_1 - \Delta R_1/2)\epsilon} | n_2' \rangle e^{-\frac{i}{\hbar}(\bar{P}_2 - \bar{P}_1)\Delta R_1} \qquad (4.8)
\end{aligned}$$

which is essentially the Wigner transform of the product of the forward and backward diabatic incremental transition matrix elements.

Finally, we note that the expectation value of some operator $\hat{O}$ at $t = 2\epsilon$ is:

$$\langle \hat{O} \rangle_{2\epsilon} = \int dR_2 \int dR_2' \sum_{n_2} \sum_{n_2'} \langle R_2 n_2 | \hat{\rho}(2\epsilon) | R_2' n_2' \rangle \langle R_2' n_2' | \hat{O} | R_2 n_2 \rangle \tag{4.9}$$

and can be expressed using mean and difference variables and substituting in Eq. (4.5). The last phase factor, $e^{\frac{i}{\hbar}\bar{P}_2 \Delta R_2}$, in Eq. (4.5) is absorbed in the definition of the operator Wigner transform:

$$\hat{O}^W_{n_2', n_2}(\bar{R}_2, \bar{P}_2) = \int d\Delta R_2 \langle \bar{R}_2 - \frac{\Delta R_2}{2} n_2' | \hat{O} | \bar{R}_2 + \frac{\Delta R_2}{2} n_2 \rangle e^{\frac{i}{\hbar}\bar{P}_2 \Delta R_2} \tag{4.10}$$

Giving:

$$\begin{aligned} \langle \hat{O} \rangle_{2\epsilon} &= (2\pi\hbar)^{2d} \int d\bar{R}_2 \int d\bar{P}_2 \int d\bar{R}_1 \int d\bar{P}_1 \int d\bar{R}_0 \sum_{n_2} \sum_{n_2'} \sum_{n_1} \sum_{n_1'} \hat{O}^W_{n_2', n_2}(\bar{R}_2, \bar{P}_2) \\ &\quad \times \delta(\bar{P}_2 \epsilon / M - (\bar{R}_2 - \bar{R}_1)) F_{n_2, n_2', n_1, n_1'}(\bar{P}_2, \bar{R}_1, \bar{P}_1, \epsilon) \\ &\quad \times \delta(\bar{P}_1 \epsilon / M - (\bar{R}_1 - \bar{R}_0)) \rho^W_{n_1 n_1'}(\bar{R}_0, \bar{P}_1) \end{aligned} \tag{4.11}$$

For completeness, the expectation value of the operator at a time $t = N\epsilon$ is given by:

$$\begin{aligned} \langle \hat{O} \rangle_{N\epsilon} &= (2\pi\hbar)^{2Nd} \int d\bar{R}_0 \prod_{\xi=1}^{N} \Big\{ \int d\bar{R}_\xi \int d\bar{P}_\xi \sum_{n_\xi} \sum_{n_\xi'} \Big\} \hat{O}^W_{n_N', n_N}(\bar{R}_N, \bar{P}_N) \\ &\quad \times \prod_{\xi=1}^{N} \Big\{ \delta(\bar{P}_\xi \epsilon / M - (\bar{R}_\xi - \bar{R}_{\xi-1})) \Big\} F_{n_\xi, n_\xi', n_{\xi-1}, n_{\xi-1}'}(\bar{P}_\xi, \bar{R}_{\xi-1}, \bar{P}_{\xi-1}, \epsilon) \\ &\quad \times \rho^W_{n_1 n_1'}(\bar{R}_0, \bar{P}_1) \end{aligned} \tag{4.12}$$

4.3 Implementation

One could imagine implementing Eq. (4.12) or the generalization of Eq. (4.5) by first sampling a point $(\bar{R}_0, \bar{P}_1)$ in the phase space of the continuous variables from the initially occupied, Wigner transformed reduced density matrix element $\rho^W_{n_1 n_1'}(\bar{R}_0, \bar{P}_1)$. Substituting this initial phase space point into the first δ-distribution on the far right enables us to perform the integral over $\bar{R}_1$ and obtain a single value of $\bar{R}_1$ deterministically thus performing the "kinetic" part of the first propagation step ϵ. The final or "potential" part of the first time step involves treating the function F in the same way as we treated the δ-distribution in the first part of the step, that is, we regard it as a distribution for $\bar{P}_2$ which depends on the already specified values of $(\bar{R}_1, \bar{P}_1)$, there are, however, two complicating features of this interpretation: First, the function F is **not**, in general, a δ-distribution which means that we must integrate over the distribution of $\bar{P}_2$ values leading to a probabilistic implementation of this part of the time step. The second complicating factor is analogous to the first in that, in fact we have multiple distributions delineated by the state labels (n_2, n_2') over which we must sum resulting in a dispersion in quantum state label space similar to the dispersion in $\bar{P}_2$ outlined above. The momentum dispersion gives rise to "nuclear" quantum tunneling and zero point effects in the continuous variables, while the sums over different endpoint states accounts for discrete quantum subsystem state transitions.

In order to proceed we need to make an approximation based on which of these effects are most important for a realistic treatment of the problem of interest. Mixed quantum-classical approaches take the momentum distribution function, which is

$F_{n_2,n_2',n_1,n_1'}$ in our case, as some form of a δ-distribution enabling $\bar{P}_2$ to be obtained uniquely, and deterministically from $(\bar{R}_1, \bar{P}_1)$ provided we have some specification for the endpoint state labels (n_2, n_2'). These methods thus suppose that the dispersion in state label space is important to capture quantum subsystem transition effects, but that momentum dispersion in the continuous variables can be sacrificed to give an implementable algorithm.

4.3.1 Momentum distribution function and state labels

The simplest form to assume for $F_{n_2,n_2',n_1,n_1'}$ to obtain deterministic dynamics for the nuclear momentum is:

$$F_{n_2,n_2',n_1,n_1'}(\bar{P}_2, \bar{R}_1, \bar{P}_1, \epsilon) = A_{n_2,n_2',n_1,n_1'}(\bar{R}_1)\delta((\bar{P}_2 - \bar{P}_1)/\epsilon - f_{n_2,n_2',n_1,n_1'}(\bar{R}_1)) \tag{4.13}$$

which is the same form as that obtained by linearizing in the difference between forward and backward nuclear variables. Inverse Fourier transforming both sides readily gives expressions for the "forces" and amplitudes of the form:

$$\begin{aligned} f_{n_2,n_2',n_1,n_1'}(\bar{R}_1)) &= \lim_{\epsilon\rightarrow 0}\lim_{\eta\rightarrow 0}\frac{\hbar}{\epsilon\eta}\mathrm{Im}\Big\{ log\langle n_2|e^{-\frac{i}{\hbar}\hat{h}(\bar{R}_1+\eta/2)\epsilon}|n_1\rangle \\ &\quad + \log\langle n_1'|e^{\frac{i}{\hbar}\hat{h}(\bar{R}_1-\eta/2)\epsilon}|n_2'\rangle - log(A_{n_2,n_2',n_1,n_1'}/(2\pi\hbar)^d)\Big\} \qquad (4.14) \\ A_{n_2,n_2',n_1,n_1'}(\bar{R}_1) &\sim \langle n_2|e^{-\frac{i}{\hbar}\hat{h}(\bar{R}_1)\epsilon}|n_1\rangle\langle n_1'|e^{\frac{i}{\hbar}\hat{h}(\bar{R}_1)\epsilon}|n_2'\rangle \qquad (4.15) \end{aligned}$$

Provided we have the end point state labels (n_2, n_2') we can use Eq. (4.14) to determine the end point $\bar{P}$ given the conditions at the previous step. To obtain (n_2, n_2') we use Monte Carlo sampling, choosing the end point labels with probability $A_{n_2,n_2',n_1,n_1'}(\bar{R}_1)/\sum_\eta |A_{\eta,\eta',n_1,n_1'}(\bar{R}_1)|$, thus maintaining the dispersion in the state label space. Transition matrix elements such as $\langle n_2|e^{-\frac{i}{\hbar}\hat{h}(\bar{R}_1)\epsilon}|n_1\rangle$ can be obtained by inserting a complete set of eigenstates between the operator and state vector and evaluating, however this will be nontrivial for systems in many dimensions, thus we make use of the mapping Hamiltonian formalism [33, 37, 64, 66] to aid in our calculation.

4.3.2 Mapping formalism

The main idea of the mapping formalism is to replace the evolution of the quantum subsystem with the evolution of a system of fictitious oscillators. The state mapping is given by:

$$|\eta\rangle \rightarrow |m_\eta\rangle = |0_1, ..., 1_\eta, ..0_n\rangle \tag{4.16}$$

where the n diabatic states are mapped onto n oscillators with a maximum of one quantum of excitation in a single oscillator. The projection operators in the system Hamiltonian, Eq. (4.2), are replaced with creation and annihilation operators of the mapping oscillator excitation:

$$|\eta\rangle\langle\eta'| \rightarrow \hat{a}_\eta^\dagger \hat{a}_{\eta'} \tag{4.17}$$

which obey bosonic commutation rules, $[\hat{a}_{\eta'}, \hat{a}_\eta^\dagger] = \delta_{\eta',\eta}$, and can be expressed in terms of the positions and momenta operators:

$$\hat{a}_{\eta'} = \frac{1}{\sqrt{2\hbar}}(\hat{q}_{\eta'} + i\hat{p}_{\eta'}) \tag{4.18}$$

The nuclear propagation is unaffected by this mapping, and the entire system Hamiltonian becomes:

$$\hat{H} \rightarrow \hat{H}_m = \hat{P}^2/2M + \hat{h}_m(R) \tag{4.19}$$

where

$$\hat{h}_m(\hat{R}) = \frac{1}{2}\sum_{\eta} h_{\eta,\eta}(\hat{R})(\hat{q}_\eta^2 + \hat{p}_\eta^2 - \hbar) + \frac{1}{2}\sum_{\eta,\eta'} h_{\eta,\eta'}(\hat{R})(\hat{q}_{\eta'}\hat{q}_\eta + \hat{p}_{\eta'}\hat{p}_\eta) \tag{4.20}$$

The quantum subsystem Hamiltonian is now a function of position and momenta of oscillators that move in a time dependent field due to the motion of the bath. Their motion is governed by Hamilton's equations:

$$\begin{aligned} \frac{dq_\beta}{dt} &= h_{\beta,\beta}(R)p_\beta + \sum_{\lambda\neq\beta} h_{\beta,\lambda}(R)p_\lambda \\ \frac{dp_\beta}{dt} &= -h_{\beta,\beta}(R)q_\beta - \sum_{\lambda\neq\beta} h_{\beta,\lambda}(R)q_\lambda \end{aligned} \tag{4.21}$$

The quantum state transition amplitudes can be obtained exactly due to the quadratic nature of the mapping Hamiltonian. Using the Herman-Kluk representation [20], which uses coherent states, and simplifying the expression using Hamilton's equations gives [7]:

$$\langle m_{\eta_i}|e^{-\frac{i}{\hbar}\epsilon\hat{h}_m(R_i)}|m_{\eta_{i-1}}\rangle = \int dq_0 dp_0 r_{t,\eta_i}(R_i)e^{-i\theta_{t\eta_i}(R_i)}r_{01_{i-1}}e^{i\theta_{0,\eta_{i-1}}}G_0 \tag{4.22}$$

where the mapping variables have been written in polar representation

$$\begin{aligned} r_{\eta_i}(R_i) &= \sqrt{q_{\eta_i}^2(R_i) + p_{\eta_i}^2(R_i)} && (4.23) \\ \theta_\eta(R_i) &= \tan^{-1}\left(\frac{p_{\eta_i}(R_i)}{q_{\eta_i}(R_i)}\right) && (4.24) \end{aligned}$$

and $G_0 = e^{-\frac{1}{2}\sum_\lambda(q_{0,\lambda}^2 + p_{0,\lambda}^2)}$. The integral over the initial conditions in Eq. (4.22) can be simplified using focused initial conditions [6] obtained by a steepest descent analysis. With focused conditions, occupied states are initialized with r on the unit circle, unoccupied states are initialized to zero, and the transition amplitude is easily obtained by evolving the state variables with Hamilton's equations.

The end point state labels (n_2, n'_2) can now be Monte Carlo sampled using probabilities given by the r values as defined in Eq. (4.23). State label n_2 is chosen with probability $r_2(R)/\sum_\eta r_\eta(R)$, and n'_2 is chosen independently by a similar equation for the backward propagated variables. Multiplying these two probabilities gives the same result as for A_{n_2,n'_2,n_1,n'_1} in Eq. (4.15). Once the end states have been chosen, $\bar{P}$ at the end point is determined by Eq. (4.14) and Eq. (4.13).

4.4 Algorithm

The expectation value of an observable is given by Eq. (4.12) and we outline our algorithm for computing this result below:

1. Choose η_0, η'_0, and sample $(\bar{R}_0, \bar{P}_1)$ from the Wigner transform of the initial density matrix.
2. Evolve the mapping variables using Hamilton's equations, Eqs. (4.21).
3. Calculate the transition matrix elements A_{n_2,n'_2,n_1,n'_1} given by Eq. (4.15) and Eq. (4.22).
4. Choose the end state label (n_2, n'_2) with probability $A_{n_2,n'_2,n_1,n'_1}(\bar{R}_1)/\sum_\eta |A_{\eta,\eta',n_1,n'_1}(\bar{R}_1)|$.
5. Determine the force $f_{n_2,n'_2,n_1,n'_1}(\bar{R}_0)$ given by Eq. (4.14).
6. Advance the nuclear position $\bar{R}$ using $\bar{R}_1 = \bar{R}_0 + \epsilon\bar{P}_1/M + f_{n_2,n'_2,n_1,n'_1}(\bar{R}_0)\epsilon^2/M$.
7. Advance the nuclear momentum using: $\bar{P}_2 = \bar{P}_1 + \epsilon f_{n_2,n'_2,n_1,n'_1}(\bar{R}_1)/2$, which is the first half step of a velocity Verlet implementation for updating the momenta.

8. Determine the force $f_{n_2,n_2',n_1,n_1'}(\bar{R}_2)$ at the new position.

9. Advance the nuclear momentum using: $\bar{P}_2 = \bar{P}_1 + \epsilon f_{n_2,n_2',n_1,n_1'}(\bar{R}_2)/2$, which is the second half velocity Verlet step.

10. Accumulate weights and phases and iterate from 2. until the final time is reached.

11. Iterate from 1. until convergence.

4.5 Discussion

We now have a method, which we call ISLAND-Map (Iterative Scheme for implementing the Linearized Approach for Nonadiabatic Dynamics in the Mapping Hamiltonian representation), to propagate the reduced density matrix forward in time that is based on a time stepping procedure combining forward and backward incremental propagators. The continuous variables are evolved deterministically with classical-like equations as can be seen from Eqs. (4.12) and (4.13), while the sums over quantum states are handled by a Monte Carlo surface hopping-like procedure with probabilities determined by the mapping variable evolution. Retaining the appropriate weights and phases for a given trajectory using Eq. (4.12), and summing over trajectories gives the expectation value of a given operator.

This method combines elements from both the Wigner-Liouville [29] and linearized method [6, 7, 8] discussed in Chapter 3. Like the Wigner-Liouville method, it propagates the entire reduced density matrix and selects the state labels through Monte Carlo sampling. One benefit is that it is much easier to implement and we expect will not require the use of filters. Like the linearized approach, ISLAND-Map uses mapping variables to describe the quantum state and combines forward and backward propagators. ISLAND-Map, however, uses an effective linearization in the short time limit, where it is expected to be reliable, as opposed to linearization for all time. It also uses mapping variable transition amplitudes to determine the state label. This avoids "ghost" trajectories, or trajectories of approximately zero weight, as well as an observable dependent force, both of which occur in the linearized approach.

There is also a fundamental difference in the types of realistic phenomena that can be described with ISLAND-Map as compared with the linearized procedure discussed in Chapter 3. In particular, with the linearized method, a given initial condition of the nuclear degrees of freedom results in only a single unique trajectory. The decoherence then results from interference between different initial conditions. In general this is only part of the story and an unrealistic description. In our new approach, a single initial condition for the nuclear variables may branch stochastically into many different alternatives which can interfere with each other, giving an additional source of decoherence. Thus, ISLAND-Map is able to model the decoherence associated with a single initial condition, as well as the decoherence arising from different initial conditions. We are currently testing this method on model condensed phase systems.

In the next chapter, we turn to the study of quantum phase transitions. We will use field theoretic techniques and purely classical simulation.

Chapter 5

Dimerized Mott insulators and quantum criticality

5.1 Introduction

The remainder of this thesis explores properties of 2-d systems near a quantum critical point, and this chapter contains background material. We discuss phase transitions, coupled dimer antiferromagnets, and the bond operator approach.

5.2 Phase transitions: classical and quantum

Phase transitions are a common occurrence in every day life, from the boiling of water to the melting of ice. Transitions occur by tuning some control parameter, such as temperature or pressure, and involve a qualitative change in the physical properties of the system. For these examples, the order is destroyed by thermal fluctuations;

hydrogen bonds are broken as water boils, the crystal structure of ice is destroyed upon melting. A less common example is a metal's transition to a superconducting state as the temperature is lowered. Again, thermal fluctuations destroy the order.

Recently, a different kind of phase transition, a quantum phase transition [51], has become a topic of great interest. These transitions take place at zero temperature, and are accessed by tuning a non-thermal control parameter, such as doping, pressure, or magnetic field. Order is destroyed by quantum fluctuations rooted in the Heisenberg uncertainty principle, as opposed to thermal fluctuations. Even though quantum phase transitions occur at zero temperature, the quantum critical behavior can influence properties at a range of temperatures. Quantum fluctuations are quite different from thermal fluctuations, and thus new theories are needed to describe these transitions. [74]

Phase transitions are traditionally classified as either first or second order. At a first order transition, the two phases co-exist. Examples include water boiling and ice melting. Second order (or continuous) transitions, on the other hand, do not have co-existing phases, and are usually characterized by an order parameter that is zero in the disordered phase and non-zero in the other. The order parameter in a ferromagnet, for example, is spin. Starting in the ordered state, a phase transition occurs upon heating when the thermal fluctuations destroy the ordering of the magnetic moments. This transition is continuous in the sense that the magnetization vanishes continuously. [16] In what follows, we consider second order, or continuous, transitions.

The transition point of a second order phase transition is also called the critical point. Close to the critical point, these systems have diverging correlation lengths, and can be described by field theories. [16, 80] In the disordered phase, the thermodynamic average of the order parameter is zero but its fluctuations are non-zero. Near the critical point, the correlation length ξ of the order parameter diverges as

$$\xi \sim |t|^{-\nu} \tag{5.1}$$

where ν is the critical exponent for the correlation length and t is a dimensionless measure of the distance from the critical point. There are also long-range correlations in time which diverge as

$$\tau_c \sim \xi^z \tag{5.2}$$

where z is the dynamical critical exponent. Close to the critical point the only length and time scales are ξ and τ_c, and the system behavior is characterized entirely by the critical exponents. The physical properties of the system are thus unchanged if, for example, all lengths in the system are rescaled and at the same time the external parameters are adjusted so the correlation length remains unchanged, giving scaling laws.

Whether quantum mechanics is important or not depends on the relative energy scale of the quantum fluctuations to the thermal energy. Since the time scale goes to infinity near the critical point, the frequency scale goes to zero as

$$\hbar\omega_c \sim |t|^{\xi z} \tag{5.3}$$

and quantum mechanics will be important as long as this energy scale is larger than $k_B T$. [74]

5.3 Dimerized Mott insulators

Mott insulators undergo a continuous quantum phase transition between a paramagnetic state and an ordered state by tuning a control parameter such as pressure or magnetic field. A number of insulators have been studied near the quantum critical point, including $C_4H_{12}N_2Cu_2Cl_6$ (PHCC) which we will discuss in Chapters 6 and 7.

Dimerized Mott insulators have an even number of $S = 1/2$ spins per unit cell, and have a gap to all spin excitations. They can be described by the bond operator method [52].

Coupled dimer antiferromagnet

We will consider a simple two-dimensional model of a Heisenberg antiferromagnet consisting of spins of $S = 1/2$. The coupled dimer Hamiltonian is given by [15]:

$$H_d = J \sum_{<ij>\epsilon A} \mathbf{S}_i \cdot \mathbf{S}_j + \lambda J \sum_{<ij>\epsilon B} \mathbf{S}_i \cdot \mathbf{S}_j \tag{5.4}$$

where $J > 0$ and $0 \leq \lambda \leq 1$. The $\mathbf{S}_j$ are spin-1/2 operators on the lattice sites. The A links form dimers, and the B links couple the dimers. This is shown in Fig 5.1. We will see that the system can be tuned across a quantum phase transition by adjusting the control parameter λ.

Phases

When $\lambda = 1$, all links are equivalent and H_d is equal to the square lattice antiferromagnet, which has long range Néel order in the ground state. Spin rotation symmetry is broken, and the spins have nonzero expectation value at each lattice

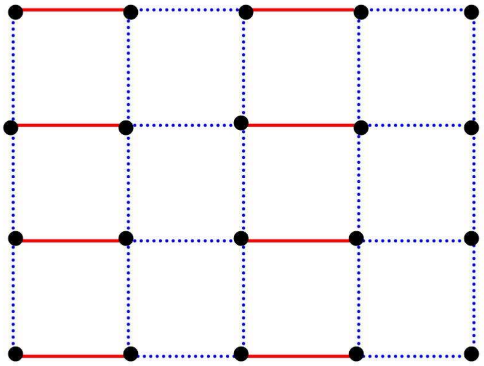

Figure 5.1: Coupled dimer antiferromagnet with spins on the lattice sites. A links are solid lines, and B links are dotted lines.

point with alternating sign, given by

$$\langle \mathbf{S}_j \rangle = \eta_j N_0 \mathbf{n} \tag{5.5}$$

where $\mathbf{n}$ is a fixed unit vector, η_j is ± 1, and N_0 is the Néel order parameter. [49] This case is shown in Fig 5.2.

The low lying excitations above the ground state are spin waves. These excitations can carry arbitrarily low energy (the phase is "gapless").

On the other hand, when $\lambda = 0$, the A links are decoupled from each other. H_d describes decoupled dimers, and the spins in each dimer pair into singlet states. This leads to a paramagnetic state which preserves spin rotation symmetry. This is shown in Fig 5.3. Excitations are formed by breaking a valence bond and forming an $S = 1$ excitation, shown in Fig 5.4. Unlike spin waves, these excitations are gapped. [49]

When $\lambda = 0$, the broken bond is localized since the A links are decoupled from each other. When λ is finite, however, it can hop from site to site, forming a $S = 1/2$ excitation [56]. See Fig 5.5. The spinons are connected by a string of weaker bonds,

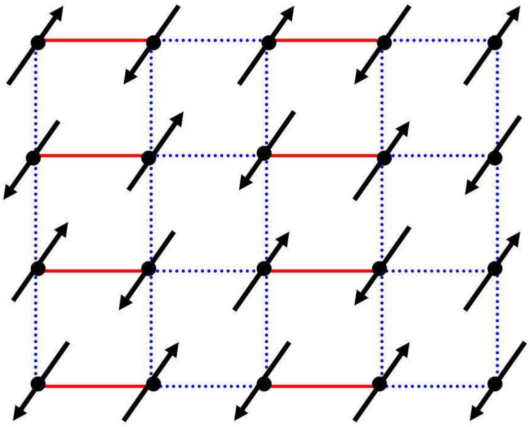

Figure 5.2: Néel order. A and B links are equivalent.

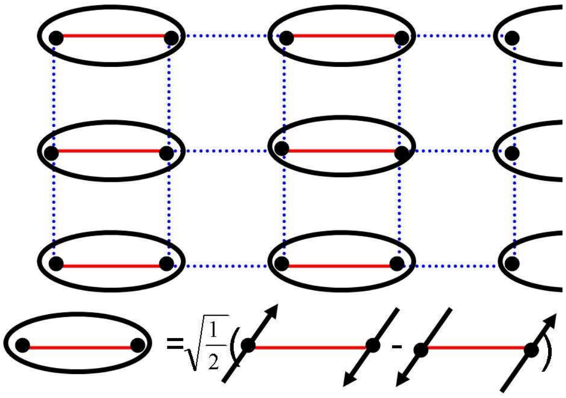

Figure 5.3: Paramagnetic state, made up of spin singlets. The A links are completely decoupled from one another.

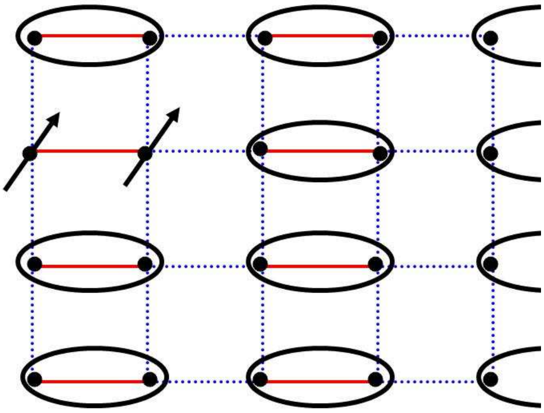

Figure 5.4: $S = 1$ excitation of the paramagnetic state.

which leads to confinement.

The distinct symmetries between the $\lambda = 1$ and $\lambda = 0$ cases mean that the two cannot be continuously connected. A phase transition occurs at an intermediate value of $\lambda = \lambda_c$ [15]. The spin gap vanishes as λ is increased from 0, while the Néel order parameter vanishes as λ is decreased from 1.

Bond operators

The bond operator method can be used to develop a continuum description of the low energy excitations near the critical point, λ_c [52]. The coupled dimer Hamiltonian, H_d, is rewritten using bosonic operators that reside on the centers of the A links. The four different states which can reside on an A link are $|\uparrow\uparrow\rangle$, $|\downarrow\downarrow\rangle$, $|\uparrow\downarrow\rangle$, $|\downarrow\uparrow\rangle$. The singlet s and triplet t bosons are given by:

$$\begin{aligned} s^\dagger|0\rangle &= (|\uparrow\downarrow\rangle - |\downarrow\uparrow\rangle)/\sqrt{2} \\ t_z^\dagger|0\rangle &= (|\uparrow\downarrow\rangle + |\downarrow\uparrow\rangle)/\sqrt{2} \end{aligned}$$

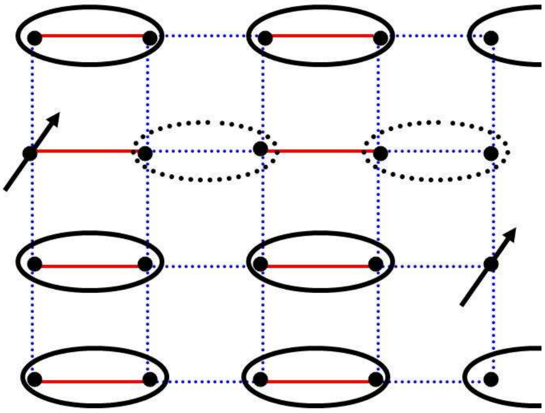

Figure 5.5: Separation of $S = 1$ excitation into two $S = 1/2$ spinons. This can only occur for a non-zero value of λ, since at $\lambda = 0$ the A links are completely decoupled.

$$\begin{aligned} t_+^\dagger|0\rangle &= -|\uparrow\uparrow\rangle \\ t_-^\dagger|0\rangle &= |\downarrow\downarrow\rangle \end{aligned} \tag{5.6}$$

where $|0\rangle$ is a reference vacuum state. The states are constrained to be either singlets or triplets: $s^\dagger s + t_\alpha^\dagger t_\alpha = 1$, where $\alpha = x, y, z$.

The spin operators S on the ends of the links are then given by:

$$\begin{aligned} \mathbf{S}_{1\alpha} &= \frac{1}{2}(s^\dagger t_\alpha + t_\alpha^\dagger s - i\epsilon_{\alpha\beta\gamma} t_\beta^\dagger t_\gamma) \\ \mathbf{S}_{2\alpha} &= \frac{1}{2}(-s^\dagger t_\alpha - t_\alpha^\dagger s - i\epsilon_{\alpha\beta\gamma} t_\beta^\dagger t_\gamma) \end{aligned} \tag{5.7}$$

which can be obtained by considering matrix elements such as $\langle s|\mathbf{S}_1|t_\alpha\rangle$ etc. We use the Einstein convention, and ϵ is the antisymmetric tensor. These spin operators can be inserted into Eqn. 5.4 to give H_d in terms of bond bosons. In all phases the s boson is condensed, so we only need to consider the t bosons to obtain a description of the system, and the condensation of the t bosons corresponds to the quantum phase transition between the paramagnetic and Néel phases. [52]

Near this critical point, the t bosons can be expanded about the wavevector corresponding to the minimum energy to obtain an effective action. This action can be rewritten by decomposing t into real and imaginary parts, $t_\alpha \sim \varphi_\alpha + i\pi_\alpha$, and integrating out the imaginary parts. Please see Reference [49] for the details. Here we present the form of the result:

$$S_{eff} = \int d^2 r d\tau (\frac{1}{2}\{(\partial_\tau \varphi_\alpha)^2 + c_x^2(\partial_x \varphi_\alpha)^2 + c_y^2(\partial_y \varphi_\alpha)^2 + r\varphi_\alpha^2\} + u(\varphi_\alpha^2)^2) \tag{5.8}$$

where the coefficients are associated with the lattice couplings. φ_α is the order parameter, and u is a dimensionless coupling constant which describes the self-interactions of the fluctuations. r is the bare "mass" of the order parameter fluctuations used to tune the system across a transition. When $r < 0$ the system is in the ordered phase since $< \varphi_\alpha > \neq 0 \propto N_0$, where N_0 is the Néel order parameter. We see that the system is described by an effective ϕ^4 field theory.

Applied magnetic field

An applied magnetic field can be used to tune the system through a phase transition, and we look at its effects. The Hamiltonian becomes:

$$H_d \rightarrow H_d - \sum_j \mathbf{B} \cdot \mathbf{S}_j \tag{5.9}$$

where B is the applied magnetic field, which breaks the spin rotation symmetry of the system. Strong fields may also lead to broken translational symmetry. [49] We consider weak fields where B is less than the energy gap and translational symmetry is preserved.

The ground and excited state wavefunctions remain insensitive to B since the added term commutes with the original Hamiltonian. The energy of the excited

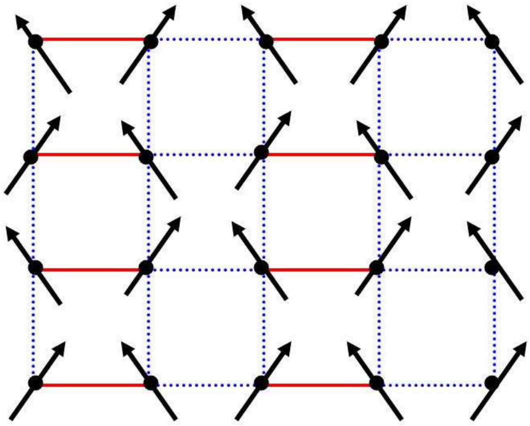

Figure 5.6: In a magnetic field, the ordered state has canted order.

states, however, are Zeeman split:

$$\varepsilon_k \rightarrow \varepsilon_k - mB \tag{5.10}$$

with $m = 0, \pm 1$ The action remains unchanged except for [1]:

$$(\partial_\tau \varphi_\alpha)^2 \rightarrow (\partial_\tau \varphi_\alpha + i\epsilon_{\alpha\beta\gamma} B_\beta \varphi_\gamma)^2 \tag{5.11}$$

which looks like Bloch precession in a magnetic field.

In a magnetic field, the paramagnetic state is the same as the $B = 0$ case. The ordered state, with $m = 1$ triplon condensation, however, now has canted order. See Fig 5.6.

From Eq. (5.10) we see that the lowest energy triplet has positive energy as long as B is less than the minimum energy gap, $\varepsilon_{k=min}$. This is required for the paramagnetic state to be stable. When B equals the minimum energy gap, the paramagnetic state becomes unstable and a quantum phase transition occurs, corresponding to Bose condensation of the $m = 1$ triplons. [49] See Fig 5.7.

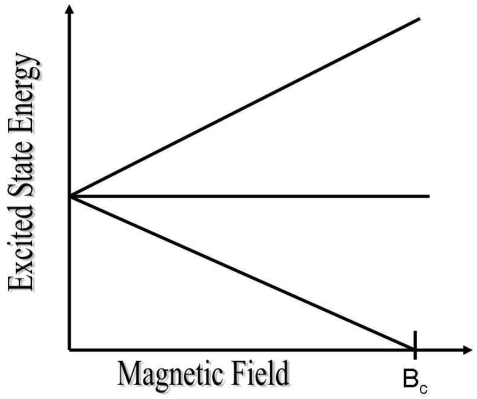

Figure 5.7: This is a plot of the excited state energy as a function of magnetic field, where the zero in energy corresponds to the ground state energy. At $B = 0$ the ground state is the paramagnetic state, and the triplet states are higher in energy. Increasing the magnetic field decreases the energy of the $m = 1$ triplet, does not affect the energy of the $m = 0$ triplet, and increases the energy of the $m = -1$ triplet. At B_c, the $m = 1$ triplet energy is equal to the paramagnetic state energy and Bose condensation of $m = 1$ triplons occurs. This corresponds to a quantum phase transition from the paramagnetic to the ordered state.

5.4 Discussion

In this chapter, we saw that coupled dimer antiferromagnets in an applied magnetic field can be described by an effective ϕ^4 quantum field theory. At the critical point, bose condensation of triplons occurs. We will explore these ideas further in Chapters 6 and 7, and also apply them to PHCC. These sections were done under the advising of Professor Subir Sachdev, and in collaboration with experimentalist Tao Hong and others [22].

Chapter 6

Field-induced quantum criticality in PHCC

6.1 Introduction

The past decade has seen much progress in the study of spin gap insulators in dimensions greater than one. Particular attention has been focused on the quantum phase transition at which the spin gap is closed by an applied magnetic field. In the vicinity of this transition, the low lying spin excitations behave like spin $S_z = 1$ canonical bosons. Measurements in the compounds $KCuCl_3$ [40], $BaCuSi_2O_6$ [58], and $NiCl_2$-$4SC(NH_2)_2$ [79], have been successfully modelled by the text-book theory of non-interacting bosons in three dimensions.

This chapter presents results of neutron scattering measurements on the two-dimensional spin gap compound piperazinium hexachlorodicuprate (PHCC), $(C_4H_{12}N_2)Cu_2Cl_6$ [68]. The temperature dependent evolution of the spectrum in the vicinity of the field-induced quantum critical point is obtained. The non-interacting Bose gas does not display a Bose condensation transition in two dimensions, and so interactions between the bosons play an essential role in the interpretation of the experiments (unlike the situation in three dimensions). We find that the energy and damping of the Bose excitations is strongly temperature (T) dependent in the quantum critical region. We also present a self-consistent Hartree-Fock theory of strongly-interacting spin excitations at quantum criticality; these theoretical results provide a good description of the measured T dependence of the excitation energies.

6.2 PHCC

PHCC has a triclinic crystal structure, with space group $P\bar{1}$, and is made up of Copper-Chlorine sheets in the **a-c** plane separated by piperazinium dication rings. The magnetic properties are dominated by Cu-Cu interactions within each sheet, mediated by Cu-Cl-Cl-Cu contacts and Cu-Cl-Cu superexchange. [68] See Figure 6.1 for a picture of a single sheet [68].

T. Hong, M. Kenzelmann, M. Stone, M. Bouloubasis, C. Broholm and D. Reich were involved in the neutron scattering experiments to map out the magnetic excitation spectrum of PHCC [22]. Measurements were taken in the vicinity of the quantum critical point at which the spin gap is closed by an applied magnetic field. They measured the energy and damping of the propagating mode above the spin gap, which becomes strongly temperature dependent at the critical field.

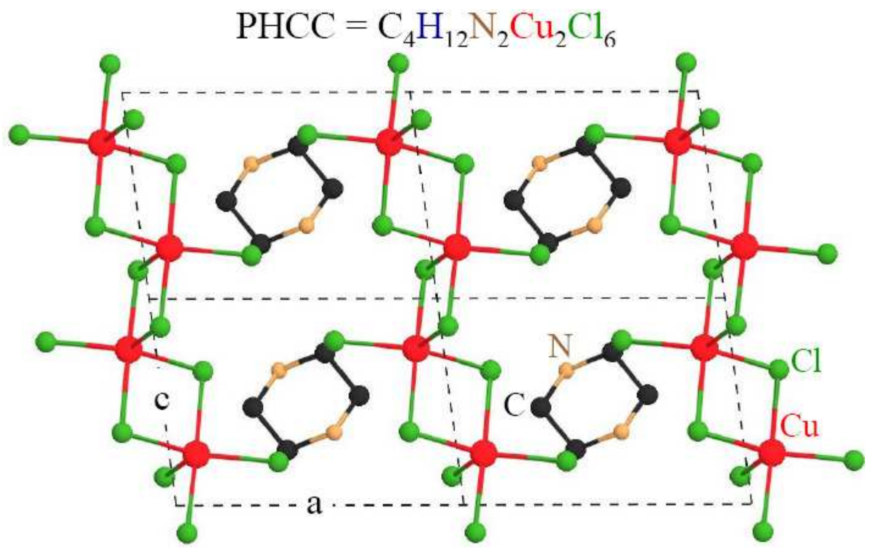

Figure 6.1: A single **a-c** plane of PHCC, displaying four unit cells.

6.3 Theory

We now turn to a description of our theoretical computations. In zero applied field, the primary excitation is a charge zero, $S = 1$ quasiparticle, often referred to as the ‘triplon’. Stone *et al.* provided an accurate determination of the dispersion of this triplon over the entire Brillouin zone; their result appears in the function $E(\mathbf{Q})$ in Eq. (9) of Ref. [68], and we will use this function in our analysis below. We are interested here in the temperature and field dependent renormalization of the triplon spectrum, in the vicinity of the quantum critical point at $H = H_c$. This renormalization clearly has its origin in the self-interactions of the triplons. In the spirit of the O(3) non-linear sigma model representation of antiferromagnets, we model this by a simple contact term. Let $S_\alpha(\mathbf{Q}, \tau)$ ($\alpha = x, y, z$) be the spin at wavevector $\mathbf{Q}$ and imaginary time τ; then, this reasoning leads to the following effective action for quantum fluctuation in the presence of a field H_α:

$$\begin{aligned}\mathcal{S} = \frac{1}{2}\int d\tau \sum_{Q} \Big(|\partial_\tau S_\alpha(\mathbf{Q},\tau) + i\epsilon_{\alpha\beta\gamma}H_\beta S_\gamma(\mathbf{Q},\tau)|^2 \\ + E^2(\mathbf{Q})|S_\alpha(\mathbf{Q},\tau)|^2\Big) + \frac{u_0}{2}\int d\tau \sum_{\mathbf{R}} \Big((S_\alpha(\mathbf{R},\tau))^2 \Big)^2 \end{aligned} \tag{6.1}$$

where $S_\alpha(\mathbf{R},\tau)$ is the spin on lattice site $\mathbf{R}$, and we have absorbed the factor of $g\mu_B$ into the definition of the field strength. We see that this is an effective ϕ^4 quantum field theory, as discussed in Chapter 5. The overall normalization of S_α has been modified to make the co-efficient of the τ derivative term above equal to unity. The self-interaction is represented by the bare quartic coupling u_0. The non-linear sigma model limit corresponds to $u_0 \to \infty$, and we will therefore be interested in the limit of large u_0.

We analyzed $\mathcal{S}$ in a self-consistent Hartree-Fock theory. Choosing H_α to be along the z direction, we take the independent components of $\mathbf{S}$ as S_z and $\psi = (S_x + iS_y)/\sqrt{2}$. The two-point correlators of these components are the dynamic spin susceptibilities, and we write these as

$$\chi_z = \frac{1}{E(\mathbf{Q})^2 + \Sigma_z - \omega^2} \tag{6.2}$$

$$\chi_{+-} = 2\chi_\psi = \frac{2}{E(\mathbf{Q})^2 + \Sigma_\psi - (\omega + H)^2} \tag{6.3}$$

$$\chi_{-+} = \frac{1}{E(\mathbf{Q})^2 + \Sigma_\psi - (\omega - H)^2}. \tag{6.4}$$

Here Σ_z and Σ_ψ are the H and T dependent self energies which we will compute below. At one-loop order, these self energies are independent of momentum and frequency.

Given the susceptibilities above, we can determine the positions of the resonance in the longitudinal and transverse susceptibilities from the location of the poles. We focus here on the minimum of the triplon dispersion, which occurs at $T = 0$ and

$H = 0$ at the wavevector (π, π) at the spin gap $\Delta_0 \equiv E(\pi, \pi)$. This triplet resonance is renormalized at finite H and T by the self energies, leading now to poles at

$$\begin{aligned} \Delta_z(H,T) &= \sqrt{\Delta_0^2 + \Sigma_z(H,T)} \\ \Delta_\psi(H,T) &= \sqrt{\Delta_0^2 + \Sigma_\psi(H,T)} - H. \end{aligned} \tag{6.5}$$

We obtain the self energies to first order by computation of one-loop graphs:

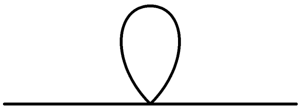

Summing over frequencies, we obtain the following expressions for the self energies:

$$\begin{aligned} \Sigma_z &= \frac{\Sigma_\psi}{2} + 20u_0 \sum_{\mathbf{Q}} \Big(\frac{n\left(\sqrt{E^2(\mathbf{Q}) + \Sigma_z}\right) + \frac{1}{2}}{\sqrt{E^2(\mathbf{Q}) + \Sigma_z}} \\ &\quad - \frac{1}{2E(\mathbf{Q})} \Big) \\ \Sigma_\psi &= \frac{\Sigma_z}{3} + \frac{40u_0}{3} \sum_{\mathbf{Q}} \Big(\frac{n\left(\sqrt{E^2(\mathbf{Q}) + \Sigma_\psi} + H\right) + 1}{\sqrt{E^2(\mathbf{Q}) + \Sigma_\psi}} \\ &\quad + \frac{n\left(\sqrt{E^2(\mathbf{Q}) + \Sigma_\psi} - H\right)}{\sqrt{E^2(\mathbf{Q}) + \Sigma_\psi}} - \frac{1}{E(\mathbf{Q})} \Big) \end{aligned} \tag{6.6}$$

where n is the Bose function

$$n(\omega) = \frac{1}{e^{\omega/T} - 1}. \tag{6.7}$$

We have assumed that the measured dispersion $E(\mathbf{Q})$ already contains the self-energy renormalizations at $T = 0$; this leads to a renormalization that is included in the expressions above, and ensures that $\Sigma_z = \Sigma_\psi = 0$ at $T = 0$.

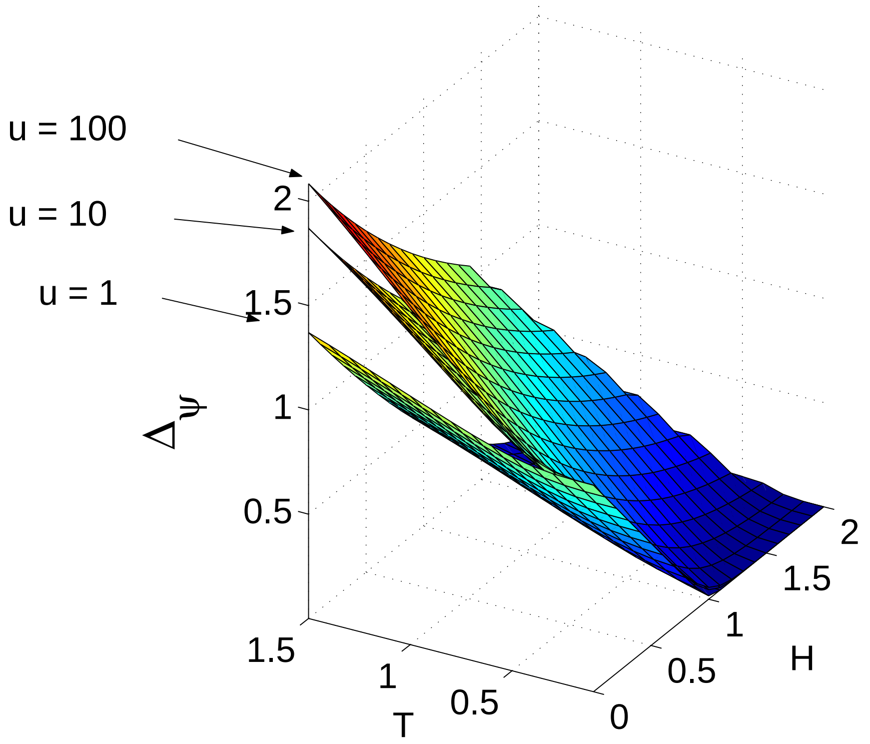

Figure 6.2: Values of Δ_ψ as a function of T and H for $u_0 = 1$, 10, 100. All parameters are in meV.

By solving Eqs (6.6) and plugging into Eqs (6.5) we obtain the energy gaps as a function of H and T. Figure 6.2 shows a plot of Δ_ψ for several values of u_0 as a function of both field and temperature. Note that once u_0 becomes large enough, the results are quite insensitive to the value of u_0.

6.4 Comparison with Experiment

Finally, we turn to a comparison between theory and experiments. For convenience, the unit of temperature T in all figures is chosen to be meV. The theoretical

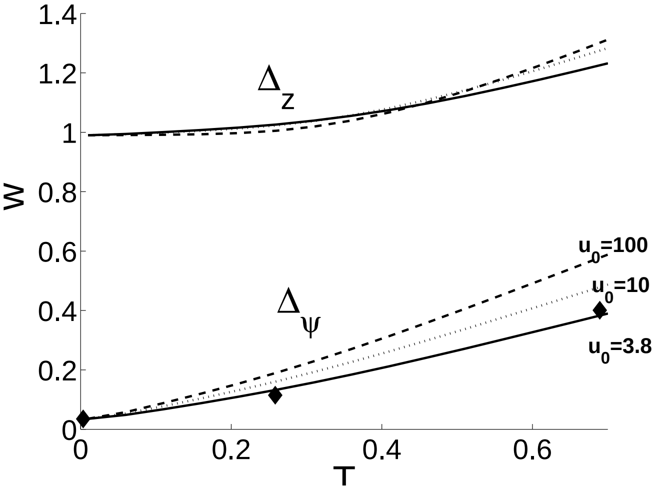

Figure 6.3: Experimental and theoretical values of Δ_ψ as a function of T at the quantum critical field $H = \Delta_0$. Solid lines are model predictions. Data points are the locations of the peak positions measured experimentally.

values of Δ_ψ from Fig 6.2 are compared with the experimental measurements of the energy of the peak neutron scattering intensity at $H = \Delta_0$ in Fig 6.3.

We also attempted to described the full neutron scattering structure factor. To obtain a direct comparison with experimental results, we augmented the response functions in Eqs. (6.2-6.4) by a phenomenological damping term: a first principles computation of this damping will be given in Chapter 7.

The dynamic structure factor, which determines the neutron scattering cross-section, is related to the susceptibilities by the fluctuation dissipation theorem:

$$\begin{aligned}
S_{zz}(\mathbf{Q}, w) &= \frac{2A}{1-e^{-w/T}} Im\chi_z \\
S_{+-}(\mathbf{Q}, w) &= \frac{2A}{1-e^{-w/T}} Im\chi_{+-} \\
S_{-+}(\mathbf{Q}, w) &= \frac{2A}{1-e^{-w/T}} Im\chi_{-+} \\
S(\mathbf{Q}, w) &= A[S_{zz} + \frac{1}{4}(S_{+-} + S_{-+})] \qquad (6.8)
\end{aligned}$$

where A is a prefactor to best fit the experimental data to the model.

The main contribution to the dynamic structure factor comes from the transverse component, $\frac{1}{4}(S_{+-} + S_{-+})$, due to the energy range probed in the experiment. The theory is presented for a range of u_0 values, and is optimized at $3.8meV^3$, however, the results are fairly insensitive to this value.

The results are shown in Fig. 6.4. The right column shows the model calculations of $S(\mathbf{Q}, w)$ at $u_0 = 3.8meV^3$ convoluted with the experimental resolution function. The top, middle, and bottom rows are for the calculation at $T = 40mK$, $3K$, and $8K$ respectively. Due to the repulsive interaction between bosons and their finite lifetime, the excitation spectrum is shifted to the higher energy side with increasing T. This is consistent with the observed neutron scattering intensity, shown in the left column.

6.5 Discussion

In summery, we studied the two-dimensional spin gap antiferromagnet PHCC near the critical point using field-theoretic techniques and comparison to experimental data. We found that the temperature dependence of the $S_z = 1$ mode is successfully described by a self-consistent Hartree-Fock theory of interacting spin excitations. In Chapter 7 we will explore the 2-d Bose gas near a quantum critical point and can apply these results to obtain the dynamic spectrum of PHCC in the continuum and classical limits [54].

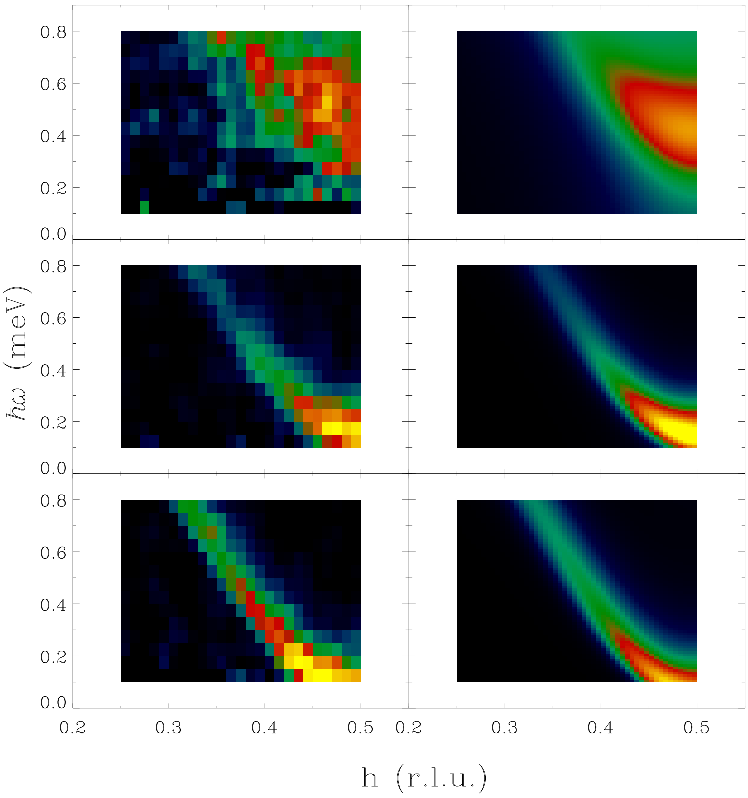

Figure 6.4: Left Column: Neutron scattering intensity measured from neutron scattering in the $(h, 0, \ell)$ plane, where $\ell = -1.35 - 0.3h$ at $H = \Delta_0 = 7.5$T. Right Column: Model predictions. Top row: $T = 8$K, $u_0 = 5$. Middle row: $T = 3$K, $u_0 = 2.5$. Bottom row: $T = 40$mK, $u_0 = 1$.

Chapter 7

Quantum critical dynamics of the two-dimensional Bose gas

7.1 Introduction

Despite the widespread recent theoretical and experimental interest in quantum phase transitions, a direct quantitative confrontation between theory and experiment has been difficult to achieve for systems in two and higher spatial dimensions. A major obstacle is that it is often difficult to tune system parameters over the range necessary to move across a quantum critical point. Furthermore, for many examples where such tuning is possible, the theory for the quantum critical point is intractable. Consequently, the analysis of the data is often limited to the testing of general scaling ansatzes, without specific quantitative theoretical predictions.

A class of quantum phase transitions have recently been exceptionally well characterized in a variety of experiments. These experiments study the influence of a strong applied magnetic field on insulating spin-gap compounds [40, 58, 79, 68, 67, 22]. The low lying spin excitations behave like spin $S_z = 1$ canonical Bose particles, and the energy required to create these bosons vanishes at a critical field $H = H_c$, which signals the position of a quantum phase transition [55] with dynamic critical exponent $z = 2$. In spatial dimensions $d = 3$, the quantum critical fluctuations are well described by the familiar Bose-Einstein theory of non-interacting bosons, and no sophisticated theory of quantum criticality is therefore necessary to interpret the experiments. The upper-critical dimension of the quantum critical point is $d = 2$, and the boson-boson interaction vanishes logarithmically at low momenta. So naively, one expects that the $d = 2$ case is also weakly coupled, and no non-trivial quantum critical behavior occurs.

The primary purpose of this chapter is to show that the above expectation for the quantum-criticality of $d = 2$ Bose gas is incorrect. While the pairwise interactions between the bosons are indeed weak, the collective properties of the finite-density, thermally excited Bose gas pose a strong-coupling problem. We will demonstrate here that an effective classical model, which can be readily numerically simulated, provides a controlled description of this problem. This will allow us to present predictions for the evolution of the dynamic spectrum of the $d = 2$ Bose gas across the quantum critical point at non-zero temperatures.

Our results can be applied to two-dimensional spin-gap antiferromagnets, in the vicinity of the gap-closing transition induced by an applied magnetic. Recent experiments [68, 67, 22] on piperazinium hexachlorodicuprate (PHCC), $(C_4H_{12}N_2)Cu_2Cl_6$, will be compared with our results in Section 7.3. These experiments are able to easily access the finite temperature quantum-critical region, which we will describe by our theory of the dilute Bose gas in $d = 2$; this Bose gas is in a regime of parameters which is typically not examined in the context of more conventional atomic Bose gas systems [43, 14].

Results similar to those presented here [42] also apply to other quantum critical points with upper-critical spatial dimension $d = 2$ *i.e.* while the zero temperature properties can be described in a weak-coupling theory, all non-zero temperature observables require solution of a strong-coupling problem. A prominent example of such a quantum-critical point is the Hertz theory of the onset of spin-density-wave order in a Fermi liquid [21]. Results for the thermodynamic and transport properties can be obtained by the methods presented here [42]. We maintain that such results are necessary for understanding experiments, and that previous theoretical results [21, 39, 38] are inadequate for a quantitative analysis.

Our results will be presented in the context of the phase diagram of the $d = 2$ Bose gas shown in Fig. 7.1 as a function of the boson chemical potential, μ, and temperature, T. At $T = 0$, there is a quantum critical point at $\mu = 0$. For $\mu < 0$, the ground state is simply the vacuum with no bosons, while for $\mu > 0$, there is a finite density of bosons in the ground state. In the spin gap antiferromagnets, $\mu = g\mu_B(H - H_c)$, where H is the applied field, H_c is the critical field, g is the gyromagnetic ratio, and μ_B is the Bohr magneton.

Fig. 7.1 presents results in terms of contours with equivalent physical properties, up to an overall energy scale (R) whose T and μ dependence will be explicitly presented below, as will the equations determining the shape of the contours. One of

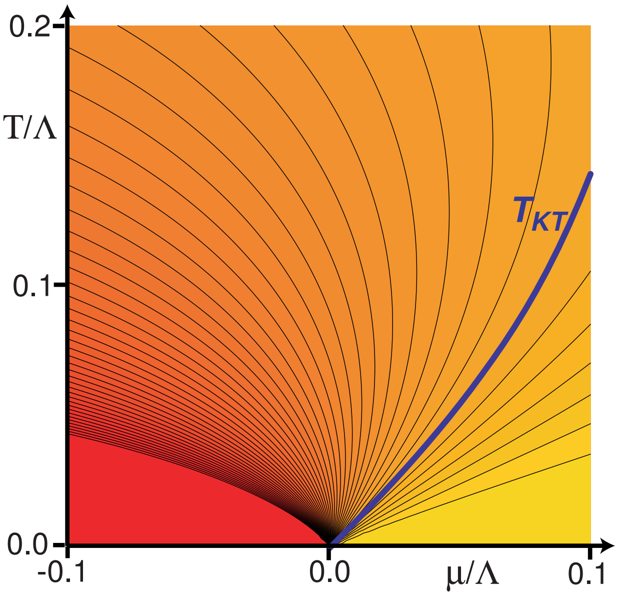

Figure 7.1: Density plot of the value of the dimensionless ratio U/R as a function of the chemical potential μ and the temperature T of a dilute Bose gas in two spatial dimensions. The energy scale U, defined in Eq. (7.3), is a measure of the pairwise interaction between the atoms, while R, defined in Eq. (7.4), is an energy scale controlling collective excitations. The physical properties of systems with the same value of U/R are the same, apart from the change in the value of the energy scale R. The Kosterlitz-Thouless transition occurs at the contour labelled T_{KT} at [50, 47] $U/R \approx 34$, and the superfluid phase is present for larger U/R. The contours shown are for equal spacings of values of R/U, with the region on the lower right including values $R/U \to 0$. Our primary results here are in the quantum critical region, with intermediate values of U/R at $\mu = 0$ and $T > 0$.

the contours is the position of the Kosterlitz-Thouless (KT) transition of the $d = 2$ Bose gas, which is present only for $\mu > 0$. We are primarily interested here in the quantum-critical region, [55] which is roughly the region with $k_B T \geq |\mu|$. In particular, we will be able to quantitatively examine the signature relaxation rate $\sim k_B T/\hbar$ of the quantum-critical regimes: the "Bose molasses" dynamics. Our results and methods also describe the crossover to the KT transition, as well as (in principle) the region with $T < T_{\mathrm{KT}}$.

7.1.1 Summary of results

We summarize here the universal aspects of our results of the quantum-critical Bose dynamics in two spatial dimensions. The continuum quantum field theory of the critical point has logarithmic corrections to scaling; consequently, the properties of the continuum theory do have a logarithmic dependence upon a non-universal ultraviolet cutoff. We will show that this cutoff dependence can be isolated within a single parameter; all other aspects of the theory remain universal, and can be accurately computed.

We will be interested in the continuum Bose gas theory with the partition function

$$\begin{aligned} \mathcal{Z}_B &= \int \mathcal{D}\psi(\mathbf{r},\tau) e^{-\mathcal{S}_B/\hbar} \\ \mathcal{S}_B &= \int_0^{\hbar/k_B T} d\tau \int d^2 r \left[\hbar \psi^* \frac{\partial \psi}{\partial \tau} + \frac{\hbar^2}{2m} \left| \nabla_{\mathbf{r}} \psi \right|^2 - \mu |\psi|^2 \right. \\ &\qquad \left. + \frac{V_0}{2} |\psi|^4 \right]. \end{aligned} \tag{7.1}$$

For PHCC, the mass m can be directly determined from the dispersion of the $S_z = 1$ excitation. We will present results primarily in the small $|\mu|$ quantum critical region of Fig 7.1, although our formalism can be extended to other regions, including across the Kosterlitz-Thouless transition into the "superfluid" phase. The bare interaction between the Bose particles, V_0, is renormalized by repeated interactions between the particles, in the T matrix, to the value

$$V_R = \frac{4\pi\hbar^2}{m\ln(\Lambda/\sqrt{\mu^2+(k_BT)^2})}, \tag{7.2}$$

where Λ is a high energy cutoff, and the square-root function in the argument of the logarithm is an arbitrary, convenient interpolating form. The parameter Λ is the sole non-universal parameter appearing in the predictions of the continuum theory. For a spin gap antiferromagnet like PHCC, we expect $\Lambda \sim J$, where J is a typical exchange constant. For our purposes, it is convenient to rescale V_R to a parameter U, which has the dimensions of energy:

$$U \equiv \frac{2mk_BT}{\hbar^2}V_R = \frac{8\pi k_BT}{(\Lambda/\sqrt{\mu^2+(k_BT)^2})}. \tag{7.3}$$

Our universal results for the continuum theory are predicated on the assumption that the logarithm in Eqs. (7.2) and (7.3) is "large". At first glance, it would appear from Eq. (7.2) that the quantum theory of the Bose gas is weakly coupled in the leading-logarithm approximation. However, as will be clear from our analysis (and has been noted in earlier works [50, 47, 48, 53]), this is *not* the case: although pairwise interactions are weak, the collective static and dynamic properties of the gas remain strongly coupled even when the logarithm is large. We shall argue, that to leading order in the logarithm, these strong coupling effects can be captured in an effective classical model. The latter model is amenable to straightforward numerical simulations, and so accurate quantitative predictions become possible, whose precision is limited only by the available computer time. Previous analyses [43, 14, 10, 11] of the dilute Bose gas in two dimensions assumed (when extended to the quantum critical region) that $\ln\ln(\Lambda/(k_B T))$ was large; a more precise version of this condition appears below, from which it is clear that this condition is essentially impossible to satisfy in practice. We will not make any assumption on the value of such a double logarithm, and only make the much less restrictive assumption on a large single logarithm.

The characteristic length and time scales of the quantum-critical Bose gas are set by a dimensionful parameter, which we denote R. Like U, we choose this to have dimensions of energy; so a characteristic length is $\hbar/\sqrt{2mR}$, while a characteristic time is $\hbar/R$. The value of R is determined by the solution of the following equation

$$R = -\mu + \frac{U}{2\pi} \ln\left(\frac{\mu}{(e^{\mu/k_B T} - 1)R}\right) . \tag{7.4}$$

Note that this defines a $R > 0$ for all $-\infty < \mu < \infty$.

To understand the magnitude of the various scales, we now discuss approximate solutions of Eqs. (7.3) and (7.4) at the quantum critical point, $\mu = 0$. The estimates below should not be used in place of the full solutions in applications of our results to experiments. For the energy scale associated with R we obtain the estimate

$$R \sim k_B T \frac{4\ln\left(\frac{1}{4}\ln(\Lambda/(k_B T))\right)}{\ln(\Lambda/(k_B T))} \quad ; \quad \mu = 0. \tag{7.5}$$

Note that the energy scale R is logarithmically smaller than $k_B T$: this will be the key in justifying an effective classical description of the dynamics. Numerically, we can easily go beyond Eq. (7.5), and obtain the full solution of Eq. (7.4) at $\mu = 0$; this is shown in Fig. 7.2. With the two dimensionful parameters, U, and R, at hand, the reader will not be surprised to learn that the effective classical theory is characterized

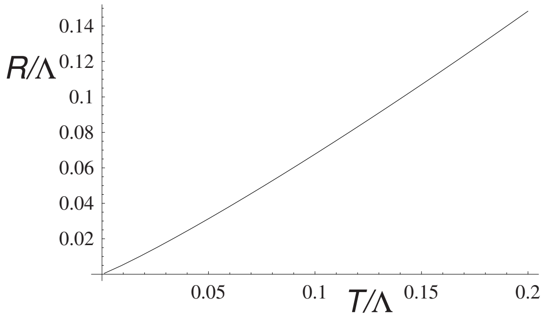

Figure 7.2: T dependence of R at the quantum critical point, $\mu = 0$, obtained by solving Eq. (7.4). Λ is a non-universal ultraviolet energy cutoff.

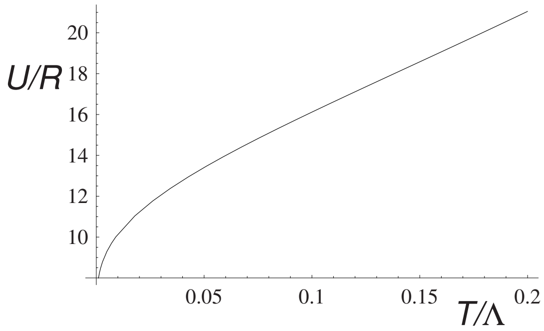

Figure 7.3: T dependence of the dimensionless ratio U/R at the quantum critical point, $\mu = 0$.

by the dimensionless coupling U/R. Indeed, as we will see, the ratio U/R behaves like an effective Ginzburg parameter for the classical theory. From Eqs. (7.4) and (7.5) we estimate

$$\frac{U}{R} \sim \frac{2\pi}{\ln\left(\frac{1}{4}\ln(\Lambda/(k_B T))\right)} \quad ; \quad \mu = 0, \tag{7.6}$$

in the quantum-critical region. Again, we can go beyond the asymptotics, and obtain precise values for U/R by numerical solution of Eqs. (7.4) and (7.3), and the result appears in Fig 7.3. So, unless $\Lambda/(k_B T)$ is astronomically large, the ratio U/R is not small, and the classical theory is strongly coupled. As we have already noted, we will not make the assumption of large double logarithms here, but instead obtain numerical results for the strongly coupled theory.

The primary result of this chapter is that the *low energy properties of the dilute Bose gas are universal functions of the ratio U/R.* This key result is illustrated in Fig 7.1 where we plot the loci of points with constant U/R, obtained from Eqs. (7.3) and (7.4). The physical properties of systems along a fixed locus are the same, apart from an overall re-scaling of energy and distance scales which are set by the value of R. In most cases, the universal dependence on U/R can be determined by straightforward numerical simulations. As has been shown earlier, in a different context [50], the effective classical model undergoes a Kosterlitz Thouless transition [50] (see Fig 7.1) at $U/R \approx 34$. The values of U/R in the quantum-critical region are smaller (see Eq. (7.6) and Fig 7.1) and the focus of our attention will be on these smaller values.

With an eye to neutron scattering observations in PHCC, we focus on the frequency dependence of the boson Green's function. In the antiferromagnet, this Green's function is proportional to the two-point spin correlation function in the plane orthogonal to the applied field *i.e.* the correlator of S_+ and S_-. The spectral density of this Green's function yields the neutron scattering cross-section. In particular, we will consider the Green's function (in imaginary time)

$$\chi_\psi(i\omega_n) = \frac{1}{\hbar}\int_0^{\hbar/k_B T} d\tau \int d^2 r e^{i\omega_n \tau} \langle \psi(\mathbf{r},\tau)\psi^*(0,0)\rangle; \tag{7.7}$$

after analytic continuation to real frequency, and application of the fluctuation-dissipation theorem, we obtain the corresponding dynamic structure factor $S_\psi(\omega)$. One of our main results is that this structure factor obeys the scaling form

$$S_\psi(\omega) = \frac{k_B T}{R^2}\Phi_\psi\left(\frac{\hbar\omega}{R}, \frac{U}{R}\right). \tag{7.8}$$

We will numerically determine the universal function Φ_ψ here for a range of values of U/R in the quantum-critical regime.

Our results for $S_\psi(\omega)$ are obtained directly in real time, and so do not suffer ambiguities associated with analytic continuation. For a significant range of values of U/R of relevance to quantum criticality, we found that our numerical results could be fit quite well with the following simple Lorentzian functional form for $\chi_\psi(\omega)$

$$S_\psi(\omega) = \frac{2k_B T}{R} Z \frac{\gamma R}{(\hbar\omega - R\omega_0)^2 + (\gamma R)^2}, \tag{7.9}$$

where the scaling form in Eq. (7.8) implies that the dimensional numbers Z, ω_0, and γ are *all universal functions of the ratio* U/R. Notice that this describes a neutron resonance at frequency $R\omega_0/\hbar$ with width $R\gamma/\hbar$; our primary purpose here is to provide theoretical predictions for the temperature dependence of these observables. Our numerical results for the values of Z, ω_0 and γ as a function of U/R appear in Figs. 7.4, 7.7, and 7.8 in later sections.

7.2 Quantum critical theory

This section will obtain the properties of the continuum theory in Eq. (7.1) which were advertized above.

The analysis of the static properties of Eq. (7.1) has been outlined in Ref. [50, 47, 48, 53]. The key step is the integrate out all the $\omega_n \neq 0$ modes of ψ to obtain an effective action only for the zero frequency component. Among the important effects of this is to replace the bare interaction V_0 by a renormalized interaction V_R obtained by summing ladder diagrams

$$V_R = \frac{V_0}{1 + (mV_0/(4\pi\hbar^2))\ln(\Lambda/(k_B T))} \approx \frac{4\pi\hbar^2}{m\ln(\Lambda/(k_B T))}. \qquad (7.10)$$

The co-efficient of $|\psi|^2$ is also renormalized, as we specify below. The resulting effective theory for the zero frequency component is most conveniently expressed by defining

$$\psi = \frac{\sqrt{2mk_B T}}{\hbar}\Psi, \qquad (7.11)$$

and rescaling spatial co-ordinates by

$$\mathbf{r} \to \frac{\hbar}{\sqrt{2m}}\mathbf{r}. \qquad (7.12)$$

This yields the following classical partition function

$$\begin{aligned} \mathcal{Z}_c &= \int \mathcal{D}\Psi(\mathbf{r}) e^{-\mathcal{S}_c} \\ \mathcal{S}_c &= \int d^2r \left[|\nabla_{\mathbf{r}}\Psi|^2 + \widetilde{R}|\Psi|^2 + \frac{U}{2}|\psi|^4 \right]. \end{aligned} \qquad (7.13)$$

Here the energy U is as defined in Eq. (7.3), while the 'mass' $\widetilde{R}$ is given by

$$\widetilde{R} = -\mu + \frac{2U}{k_B T}\int \frac{d^2k}{4\pi^2}\left(\frac{1}{e^{(k^2-\mu)/(k_B T)} - 1} - \frac{k_B T}{k^2 - \mu} \right). \qquad (7.14)$$

The most important property of this expression for $\widetilde{R}$ is that the integral of k is not ultraviolet finite, and has a logarithmic dependence on the upper cutoff. However, this is not a cause for concern. The theory $\mathcal{Z}_c$ is itself not a ultraviolet finite theory, and its physical properties do have a logarithmic dependence on the upper cutoff. Fortunately (indeed, as must be the case), the cutoff dependence in $\widetilde{R}$ above is precisely that needed to cancel the cutoff dependence in the correlators of $\mathcal{Z}_c$ so that the final physical results are cutoff independent. This important result is demonstrated by noting that the only renormalization needed to render $\mathcal{Z}_c$ finite is a 'mass' renormalization from $\widetilde{R}$ to R, as defined by

$$R \equiv \widetilde{R} + 2U \int \frac{d^2k}{4\pi^2} \frac{1}{k^2 + R}. \tag{7.15}$$

Here, the R in the propagator on the r.h.s. is arbitrary, and is chosen for convenience. We could have chosen a propagator $1/(k^2 + cR)$ where c is an arbitrary numerical constant; this would only redefine the meaning of the intermediate parameter R, but not the value of any final observable result. Combining Eq. (7.15) with Eq. (7.14), we observe that the resulting expression for R is free of both ultraviolet and infrared divergences. The momentum integrals can be evaluated, and lead finally to the expression for R already presented in Eq. (7.4).

When expressed in terms of the renormalized parameter R, the properties of the continuum theory $\mathcal{Z}_c$ are universal (*i.e.* independent of short-distance regularization). They are defined completely by the length scale $1/\sqrt{R}$ and the dimensionless ratio U/R. The field Ψ is also dimensionless, and acquires no anomalous dimension. This means *e.g.* the equal time correlations obey the scaling form

$$S(k) = \langle |\Psi(k)|^2 \rangle = \frac{1}{R} \Phi \left(\frac{k}{\sqrt{R}}, \frac{U}{R} \right), \tag{7.16}$$

where Φ is a universal function. Note that here, and in the remainder of this chapter, we have rescaled momenta corresponding to Eq. (7.12)

$$k \to \frac{\sqrt{2m}}{\hbar} k, \tag{7.17}$$

so that k^2 has the dimensions of energy. The function Φ can be easily computed in a perturbation theory in U/R, and results to order $(U/R)^2$ appear in Ref. [50].

However, we are interested in values of U/R which are not small, and for this we have to turn to the numerical method described in the following subsection.

7.2.1 Numerics: equal time correlations

We will analyze numerically $\mathcal{Z}_c$ by placing it in a square lattice of spacing a, and verifying that the correlations measured in Monte Carlo simulations become a independent and universal in the limit $a \to 0$.

The partition function on the lattice is

$$\begin{aligned} \mathcal{Z}_{cL} &= \prod_i \int d\Psi_i e^{-\mathcal{S}_{cL}} \qquad (7.18) \\ \mathcal{S}_{cL} &= \sum_{\langle ij \rangle} |\Psi_i - \Psi_j|^2 + \sum_i \left[\widetilde{R}_L a^2 |\Psi_i|^2 + \frac{Ua^2}{2} |\Psi_i|^4 \right]. \end{aligned}$$

The parameter $\widetilde{R}_L$ is *not* equal to the parameter $\widetilde{R}$ above. Instead, the mapping to the quantum theory has to be made by requiring that the values of the renormalized R are the same. In the present lattice theory we have

$$\widetilde{R}_L = R - 2U \int_{-\pi}^{\pi} \frac{dk_x}{2\pi} \int_{-\pi}^{\pi} \frac{dk_y}{2\pi} \frac{1}{4 - 2\cos(k_x) - 2\cos(k_y) + Ra^2}. \qquad (7.19)$$

We can measure lengths in units of R, and for each value of U, determine $\widetilde{R}_L$ from Eq. (7.19), and test if the Monte Carlo correlations are independent of a in the limit of small a. The resulting correlations then determine the scaling function Φ in (7.16).

We used this method to determine the values of the function $\Phi(0, U/R)$ for a sample set of values of U/R appropriate to the quantum-critical region. Note that $\Phi(0, U/R) = Z$, where Z is the amplitude appearing in the dynamic function in Eq. (7.9). We used the Wolff cluster algorithm (as described in Ref. [50]) to sample

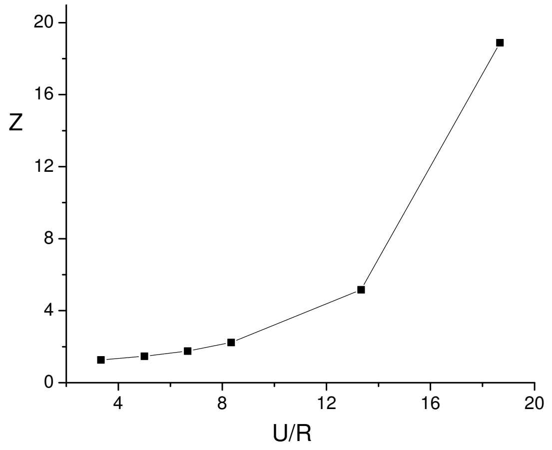

Figure 7.4: Universal dependence of the equal-time correlation at zero momentum on U/R. The parameter Z is that appearing in Eq. (7.9).

the ensemble specified by $\mathcal{Z}_{cL}$. Measurement of the resulting correlations led to the results shown in Fig 7.4.

7.2.2 Dynamic theory

We now extend the classical static theory above to unequal time correlations by a method described in some detail in Refs. [50] and [51]. As argued there, provided the scale $R < k_B T$, the unequal time correlations can also be described by classical equations of motion. In the context of perturbation theory, the reduction to classical equations of motion is equivalent to the requirement that it is a good approximation to replace all Bose functions by their low energy limit:

$$\frac{1}{e^{\omega/T}-1} \approx \frac{T}{\omega}. \tag{7.20}$$

From Eq. (7.5) we observe that the requirement on R is satisfied in the quantum-critical region. It also holds everywhere in the superfluid phase, with $\mu > 0$, where R becomes exponentially small in $1/(k_B T)$ (as can be shown from Eq. (7.4)). However, it does fail in the low T 'spin-gap' region with $\mu < 0$, where $R > k_B T$. We will not address this last region here, although a straightforward perturbative analysis of the full quantum theory is possible here, as noted in Ref. [51]. Some results on the perturbation theory appear in Appendix C.

The classical equations of motion obeyed by Ψ are merely the c-number representation of the Heisenberg equations of motion obeyed by ψ. With the rescalings in Eqs. (7.11) and (7.12), these are

$$i\hbar \frac{\partial \Psi}{\partial t} = \frac{\delta \mathcal{S}_c}{\delta \Psi^*}. \tag{7.21}$$

Following the reasoning leading to Eq. (7.16), it follows that the correlations of the Ψ evolution described by these equations of motion obey the scaling form

$$S(k,t) = \langle \Psi(k,t)\Psi^*(k,0)\rangle = \frac{1}{R}\Phi_t\left(\frac{k}{\sqrt{R}}, \frac{Rt}{\hbar}, \frac{U}{R}\right). \tag{7.22}$$

where the scaling function Φ_t can be determined numerically, as we describe below. After the rescalings in Eqs (7.11) and (7.12), we conclude that the Fourier transform of $S(k,t)$ to $S(k,\omega)$ is related to the dynamic structure factor $S_\psi(\omega)$ defined below Eq. (7.7) by

$$S_\psi(\omega) = k_B T S(0,\omega). \tag{7.23}$$

We now describe our numerical computation of Φ_t. We begin by sampling the ensemble of Ψ_i values specified by $\mathcal{Z}_{cL}$, as in the previous section. Once the ensemble is thermalized, we choose a typical set of values of Ψ_i as the initial condition. These are evolved forward in time deterministically by solving the equations of motion

$$i\frac{\partial \Psi_i}{\partial \bar{t}} = \sum_{j\ n.n.i} (\Psi_i - \Psi_j) + \widetilde{R}_L a^2 \Psi_i + U a^2 |\Psi_i|^2 \Psi_i, \tag{7.24}$$

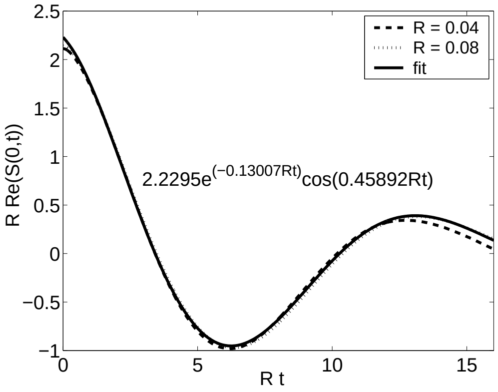

Figure 7.5: Real part of the time-dependent structure factor $S(0,t)$ obtained from our numerical simulation. The results above are for $U/R = 8.33$. Two different values of R are shown, and the axes have been scaled to demonstrate the scaling collapse as required by Eq. (7.22). The fit with the functional form in Eq. (7.26) is also shown.

where $\bar{t} = t/\hbar$. For each initial condition, this defines a $\Psi_i(\bar{t})$. Then

$$\Phi_t(0, R\bar{t}, U/R) = \frac{a^2 R}{N^2} \left\langle \Big(\sum_j \Psi_j^*(\bar{t}) \Big) \Big(\sum_\ell \Psi_\ell(\bar{t}) \Big) \right\rangle \tag{7.25}$$

for a lattice of N^2 sites, and where the average is over the ensemble of initial conditions. Sample results from such simulations appear in Figs. 7.5 and 7.6.

We have fit each observed time evolution to the functional form

$$\Phi_t \approx Z e^{-R(i\omega_0 \bar{t} + \gamma|\bar{t}|)}, \tag{7.26}$$

where Z, ω_0, γ are numbers determined from the fit. A sample fit is shown in Figs. 7.5 and 7.6. As is clear from the figures, this form provides an excellent fit over a substantial time window. Taking the Fourier transform of this result, and using Eq. (7.23), we obtain a result for $S_\psi(\omega)$ in the form in Eq. (7.9), with the same parameters Z, ω_0, γ.

The results for Z appeared earlier in Fig. 7.4, and our results ω_0 and γ as a function of U/R appears in Figs. 7.7 and 7.8. We can now combine the results in

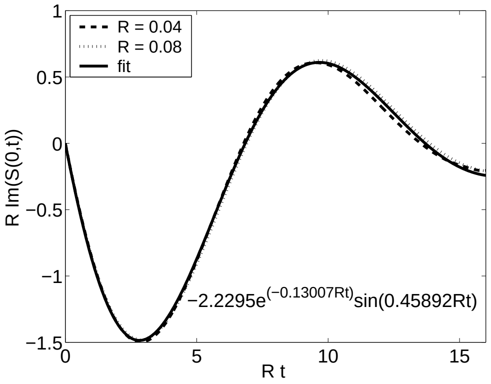

Figure 7.6: As in Fig. 7.5, but for the imaginary part of the correlation function.

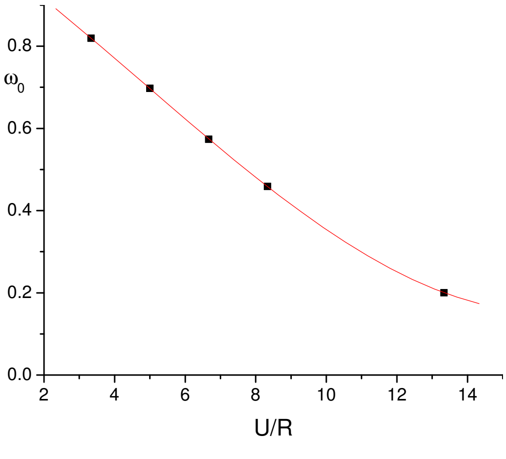

Figure 7.7: The universal dependence of the dimensionless frequency ω_0 on U/R. The points are the results of the numerical simulation, while the line is a best fit polynomial used for interpolation.

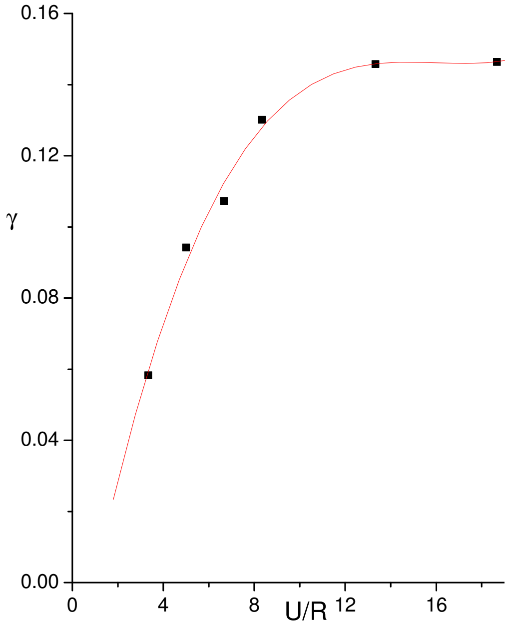

Figure 7.8: As in Fig 7.7, but for the dimensionless damping γ. The full line at small U/R is the result of the perturbation theory obtained in Eq. (C.4).

these figures with those in Fig 7.3, and obtain predictions for the T dependence of the resonant frequeny and damping in the dynamic structure factor in Eq. (7.9) at the quantum-critical point. These results appear in Fig 7.9 and 7.10.

7.3 Conclusions

We have argued that the quantum-critical dynamics of the two-dimensional Bose gas (and of other quantum critical points in two spatial dimensions) represents a strong-coupling problem. Nevertheless, an effective classical description was obtained to leading logarithmic order, allowing tractable numerical simulation. The primary results of this simulation at the quantum critical point appear in Figs. 7.9 and 7.10, which specify the parameters appearing in Eq. (7.9).

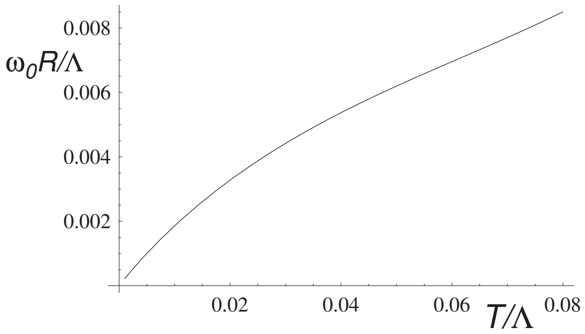

Figure 7.9: The universal dependence of the oscillation frequency $\omega_0 R$ on T at the quantum-critical point $\mu = 0$, obtained from Figs. 7.3 and 7.7.

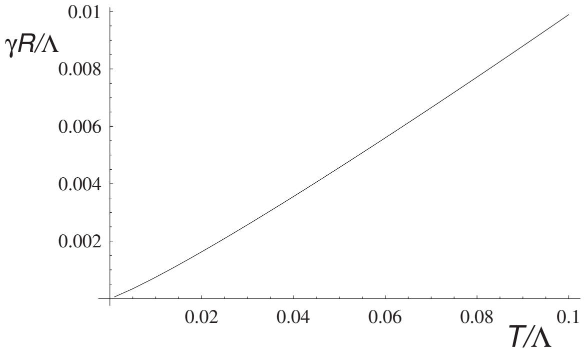

Figure 7.10: The universal dependence of the damping rate γR on T at the quantum-critical point $\mu = 0$, obtained from Figs. 7.3 and 7.8.

In comparing our results to experiments, we have to set the value of the unknown high energy cutoff Λ. For the range of parameters shown in Figs. 7.9 and 7.10, we find a roughly linear dependence of $\omega_0 R$ and γR on T, with $\omega_0 R \approx 0.11(k_B T)$ and $\gamma R \approx 0.10(k_B T)$. The experiments [68, 67, 22] on the quantum-critical point of PHCC, also observe a roughly linear dependence of peak frequency and width on temperature, but with different co-efficients; the peak frequency $\approx 0.62 k_B T$, while the width is $\approx 0.23 k_B T$. Choosing a different range of Λ for the theory, *e.g.* assuming the experiments are in the range $T/\Lambda < 0.01$, will change the theoretical predictions for $\omega_0 R$ and γR, but does not improve the agreement with experiments.

For the peak frequency, the work of Ref. [22] suggests an origin for the above discrepancy. A similar theory was used in that paper to obtain the predictions of the peak frequency, but keeping the full lattice dispersion for the spin excitations, and the quantum Bose function values for the occupation numbers: good agreement was found between such a theory and the experimental observations. The continuum and classical limits taken here were avoided.

For the width of the spin excitation, we expect that the damping is more strongly dominated by the low energy and low momentum excitations, and so the present continuum, classical theory should yield a more accurate description of the experiments. This is indeed the case, relative to the poor accuracy of the peak frequency in the continuum theory. Nevertheless, a discrepancy of a factor of ≈ 2 remains between our present quantum critical theory and the experimental observations. It is possible that taking the classical theory also on the lattice will improve agreement with experiments. However, there are also corrections to the present continuum theory which could improve the situation: in particular, at higher order in V_R, there appear renormalization of the time-derivative term in Eq. (7.1). This renormalization would change the time-scale in the classical equations of motion, and so change the overall frequency scale of the results in Figs. 7.9 and 7.10.

Appendix A

Quantum-classical Liouville equation

We start with the Liouville-von Neumann equation, which describes the time evolution of the density operator:

$$i\hbar\frac{\partial\hat{\rho}}{\partial t} = [\hat{H}, \hat{\rho}] \tag{A.1}$$

and assume the Hamiltonian to be of the form

$$\hat{H} = \frac{\hat{P}^2}{2M} + \frac{\hat{p}^2}{2m} + \hat{V}_s(q) + \hat{V}_b(R) + \hat{V}_c(q, R) \tag{A.2}$$

where small variables refer to the quantum system and large variables refer to the bath particles. $\hat{V}_c$ is the coupling between the quantum system and the bath.

The phase space representation of an operator can be constructed by taking the Wigner transform. Taking the Wigner transform of the Liouville-von Neumann equation over the bath degrees of freedom gives:

$$\frac{\partial \hat{\rho}}{\partial t} = -\frac{i}{\hbar}(\hat{H}_W(R,P)e^{\frac{\hbar\Lambda}{2i}}\hat{\rho}_W(R,P,t) - \hat{\rho}_W(R,P,t)e^{\frac{\hbar\Lambda}{2i}}\hat{H}_W(R,P)) \tag{A.3}$$

where

$$\hat{H}_W(R,P) = \frac{\hat{P}^2}{2M} + \frac{\hat{p}^2}{2m} + \hat{V}_W(q,R) \tag{A.4}$$

and

$$\Lambda = \overleftarrow{\nabla_P} \cdot \overrightarrow{\nabla_R} - \overleftarrow{\nabla_R} \cdot \overrightarrow{\nabla_P} \tag{A.5}$$

The partial Wigner transforms of an operator $\hat{A}$ and a density operator $\hat{\rho}$ are defined by [72]:

$$\hat{A}_W(R,P) = \int dz e^{iP\cdot z}\langle R - \frac{z}{2}|A|R + \frac{z}{2}\rangle \tag{A.6}$$

$$\rho_W(R,P) = (2\pi\hbar)^{-3N}\int dz e^{iP\cdot z}\langle R - \frac{z}{2}|\rho|R + \frac{z}{2}\rangle \tag{A.7}$$

Working in dimensionless units allows us to see the explicit mass dependence. Defining the dimensionless variable $\Lambda' = \frac{\Lambda\hbar}{\mu}$, where $\mu = (\frac{m}{M})^{\frac{1}{2}}$, and expanding to lowest order in μ, we obtain the mixed quantum-classical Liouville equation [24]

$$\frac{\partial \hat{\rho}_W}{\partial t} = -\frac{i}{\hbar}[\hat{H}_W, \hat{\rho}_W] + \frac{1}{2}(\{\hat{H}_W, \rho_W\} - \{\hat{\rho}_W, \hat{H}_W\}) \tag{A.8}$$

where the Poison brackets are defined by

$$\{A,B\} = \frac{\partial A}{\partial R}\cdot\frac{\partial B}{\partial P} - \frac{\partial A}{\partial P}\cdot\frac{\partial B}{\partial R} \tag{A.9}$$

We now have an equation for the time evolution of the density operator that has both operator and phase space nature. The only approximation made was truncating the expansion in μ to include terms up to linear order.

Appendix B

Trotterized Wigner-Liouville approach

This appendix describes the implementation of the Wigner-Liouville trotterized method in the adiabatic basis [29]. The solution of the quantum-classical Liouville equation is:

$$\rho_W^{\alpha\alpha'}(R,P,t) = \sum_{\beta\beta'} (e^{-i\mathcal{L}t})_{\alpha\alpha'\beta\beta'} \rho_W^{\beta\beta'}(R,P,0) \tag{B.1}$$

where $\rho_W^{\alpha\alpha'}(R,P) = \langle \alpha, R | \rho_W | \alpha', R \rangle$. This can be written in Dyson form:

$$(e^{-i\mathcal{L}t})_{\alpha\alpha'\beta\beta'} = e^{-i\mathcal{L}^0_{\alpha\alpha'}t}\delta_{\alpha\beta}\delta_{\alpha'\beta'} + \sum_{\gamma\gamma'} \int_0^t dt' e^{-i\mathcal{L}^0_{\alpha\alpha'}(t-t')} J_{\alpha\alpha'\gamma\gamma'} (e^{-i\mathcal{L}t'})^{\gamma\gamma'\beta\beta'} \tag{B.2}$$

To simplify the notation, associate s with the pair $\alpha\alpha'$. Divide the time interval into small enough time segments, $\Delta t_j = \delta$ to use the trotter approximation:

$$(e^{i\mathcal{L}t})_{s_0 s_N} = \sum_{s_1, s_2 \ldots s_{N-1}} \prod_{j=1}^{N} (e^{i\mathcal{L}\Delta t_j})_{s_{j-1}s_j} \tag{B.3}$$

where

$$(e^{i\mathcal{L}\delta})_{s_0 s_1} \approx (e^{i\mathcal{L}^0\delta/2})_{s_0 s_0} (e^{-J\delta})_{s_0 s_1} (e^{i\mathcal{L}^0\delta/2})_{s_1 s_1} \tag{B.4}$$

In this approximation, the full propagator consists of free propagation (for the bra and ket states) on a single surface, with intermittent hops between surfaces.

It will be helpful to separate the $J_{\alpha\alpha'\beta\beta'}$ operator as follows:

$$J_{\alpha\alpha'\beta\beta'} = J_{1\alpha\alpha'\beta\beta'} + J_{2\alpha\alpha'\beta\beta'} \tag{B.5}$$

where

$$J_{1ss'} = -(d_{\alpha\beta}\delta_{\alpha'\beta'} + d^*_{\alpha'\beta'}\delta_{\alpha\beta}) \cdot \frac{P}{M} \tag{B.6}$$

$$J_{2ss'} = -\frac{(E_\alpha - E_\beta)d_{\alpha\beta}\delta_{\alpha'\beta'} + (E_{\alpha'} - E_{\beta'})d^*_{\alpha'\beta'}\delta_{\alpha\beta}}{2} \cdot \frac{\partial}{\partial P} \tag{B.7}$$

and $d_{\alpha\beta}$ is the non-adiabatic coupling matrix element:

$$d_{\alpha\beta} = \langle \alpha, R|\nabla_R|\beta, R\rangle \tag{B.8}$$

Since the coupling matrix is anti-symmetric with respect to exchange of α and β, $J_{1ss'}$ is anti-symmetric with respect to interchange of s and s', and $J_{2ss'}$ is symmetric, and are therefore diagonalized by different orthogonal transformations.

$$\begin{aligned}(e^{-J\delta})_{s_0 s_N} &= \sum_{s_1 s_2} (e^{-J_1\delta/2})_{s_0 s_1} (e^{-J_2\delta})_{s_1 s_2} (e^{-J_1\delta/2})_{s_2 s_N} \\ &\equiv \sum_{s_1 s_2} (Q_1)_{s_0 s_1} (Q_2)_{s_1 s_2} (Q_1)_{s_2 s_N} \end{aligned} \tag{B.9}$$

For a two state system:

$$J_1 = \begin{pmatrix} 0 & 1 & 1 & 0 \\ -1 & 0 & 0 & 1 \\ -1 & 0 & 0 & 1 \\ 0 & -1 & -1 & 0 \end{pmatrix} \frac{P}{M} \cdot d(R) \tag{B.10}$$

Diagonalize J_1 with transformation K and exponentiate to obtain an expression for Q_1:

$$Q_1 = e^{-J_1\delta/2} = e^{-KD_1\delta/2K^{-1}} \tag{B.11}$$

Matrix elements of Q_1 contain terms of the form:

$$\pm cos^2(a), \ \ \pm sin(a)cos(a), \ \ \pm sin^2(a) \tag{B.12}$$

where $a = P/Md_{10}(R)\delta\partial/\partial P$, and are used in the selection of hops. The expression for Q_2 can be obtained in a similar manner, where

$$J_2 = -\begin{pmatrix} 0 & 1 & 1 & 0 \\ 1 & 0 & 0 & 1 \\ 1 & 0 & 0 & 1 \\ 0 & 1 & 1 & 0 \end{pmatrix} \frac{(E_1(R) - E_0(R))d(R) \cdot \frac{\partial}{\partial P}}{2} \tag{B.13}$$

Exponentiate to obtain an expression for Q_2:

$$Q_2 = e^{-J_2\delta} = e^{-K'D_2\delta K'^{-1}} \tag{B.14}$$

Matrix elements of Q_2 will contain terms of the form:

$$e^{b\cdot\frac{\partial}{\partial P}} \pm e^{-b\cdot\frac{\partial}{\partial P}} \pm 1 \tag{B.15}$$

where $b = (E_1(R) - E_0(R))d_{10}(R)\delta$. This yields small positive and negative momentum shifts, which cause branching of the trajectories.

The short time propagator can now be written as:

$$(e^{i\mathcal{L}\delta})_{s_0 s_3} = \sum_{s_1 s_2} (e^{i\mathcal{L}^0\delta/2})_{s_0 s_0} Q_{1 s_0 s_1} Q_{2 s_1 s_2} Q_{1 s_2 s_3} (e^{i\mathcal{L}^0\delta/2})_{s_3 s_3} \tag{B.16}$$

Jump Approximation

The jump approximation simplifies the calculations considerably. In its absence, when Q_2 acts on a function $f(R,P)$, there will be branching in the number of trajectories. By taking the limit of small $|b| = |(E_1(R) - E_0(R))d_{10}(R)|\delta << 1$ which can be enforced by making the time step very small, the expression for Q_2 is simplified and branching is eliminated. The result simplifies to:

$$(e^{i\mathcal{L}\delta})_{s_0s_1} = \sum_{s_1s_2}(e^{i\mathcal{L}^0\delta/2})_{s_0s_0}(Q_1)^2_{s_0s_1}T_{s_0s_1}(e^{i\mathcal{L}^0\delta/2})_{s_1s_1} \tag{B.17}$$

where T is defined as:

$$\begin{pmatrix} 1 & 1-\frac{b\hat{d}\cdot\frac{\partial}{\partial P}}{2a} & 1-\frac{b\hat{d}\cdot\frac{\partial}{\partial P}}{2a} & 1-\frac{b\hat{d}\cdot\frac{\partial}{\partial P}}{a} \\ 1+\frac{b\hat{d}\cdot\frac{\partial}{\partial P}}{2a} & 1 & 1 & 1-\frac{b\hat{d}\cdot\frac{\partial}{\partial P}}{2a} \\ 1+\frac{b\hat{d}\cdot\frac{\partial}{\partial P}}{2a} & 1 & 1 & 1-\frac{b\hat{d}\cdot\frac{\partial}{\partial P}}{2a} \\ 1+\frac{b\hat{d}\cdot\frac{\partial}{\partial P}}{a} & 1+\frac{b\hat{d}\cdot\frac{\partial}{\partial P}}{2a} & 1+\frac{b\hat{d}\cdot\frac{\partial}{\partial P}}{2a} & 1 \end{pmatrix} \tag{B.18}$$

Terms like $(1 \pm \frac{b\hat{d}\cdot\frac{\partial}{\partial P}}{2a})f(P\cdot\hat{d})$ in T change $P\cdot\hat{d}$ by $\pm\frac{b}{2a}$. Transitions that increase the energy of the system are forced not to occur.

Adiabatic states

The adiabatic states are represented in terms of a mixing angle to aid in the numerical stability. For a two state system, the adiabatic states can be written in terms of two orthogonal diabatic basis functions, $\Phi^d_{1,2}(r)$, as:

$$\begin{aligned} \Phi^a_n(r,R) &= cos[\Theta(R)]\Phi^d_1(r) + sin[\Theta(R)]\Phi^d_2(r) \\ \Phi^a_m(r,R) &= -sin[\Theta(R)]\Phi^d_1(r) + cos[\Theta(R)]\Phi^d_2(r) \end{aligned} \tag{B.19}$$

where $\Theta(R)$ depends on the bath configuration, and is the mixing angle between diabatic basis states. With this form, the coupling matrix elements are simply:

$$\langle \Phi^a_m | \nabla_R | \Phi^a_n \rangle = \nabla_R \Theta \tag{B.20}$$

when $n \neq m$. In terms of the Hamiltonian matrix elements, the mixing angle is given by:

$$\Theta = \frac{1}{2}\Big(\frac{\pi}{2} - sin^{-1}\Big(\frac{H_{22} - H_{11}}{\sqrt{(H_{22} - H_{11})^2 + 4H_{12}^2}}\Big)\Big) \tag{B.21}$$

Algorithm

The expectation value of an observable is given by:

$$\begin{aligned}
\langle O(t) \rangle \quad &= Tr' \int dRdPO_W(R,P)e^{-i\mathcal{L}t}\rho_W(R,P,0) \\
&= Tr' \int dRdPe^{i\mathcal{L}t}O_W(R,P)\rho_W(R,P,0) \\
&= \sum_{s_0 s_N} \int dRdP[(e^{i\mathcal{L}t})_{s_0 s_N} O_W^{s_N}(R,P)]\rho_W^{s_0'}(R,P,0) \\
&= \sum_{s_0 s_1 \ldots s_N} \int dRdP\rho_W^{s_0'}(R,P,0)[\prod_{j=1}^{N}(e^{i\mathcal{L}t})_{s_{j-1}s_j} O_W^{s_N}(R,P)]
\end{aligned} \tag{B.22}$$

where Tr' is the trace over the quantum subsystem, and s' is the complex conjugate of s. These multi-dimensional sums can be carried out through Monte Carlo sampling. The propagator was moved to act on the observable instead of the density matrix since this makes the sampling easier.

The sequence of transfer operations in Equation B.17 can be handled by backwards computation. Consider the following transfer operation sequence $ABCf(x)$, where:

$$
\begin{aligned}
Af(x) &= \alpha(x)f(a(x)) \\
Bf(x) &= \beta(x)f(b(x)) \\
Cf(x) &= \gamma(x)f(c(x))
\end{aligned}
\tag{B.23}
$$

Operating from left to right:

$$
\begin{aligned}
ABC(f(x_0)) &= A[BCf(x_0)] = \alpha(x_0)[BCf(x_1)], x_1 = a(x_0) \\
BC(f(x_1)) &= B[Cf(x_1)] = \beta(x_1)[Cf(x_2)], x_2 = b(x_1) \\
C(f(x_2)) &= \gamma(x_2)f(x_3), x_3 = c(x_2)
\end{aligned}
\tag{B.24}
$$

Introducing time as a parameter, ABC would calculated by going from left to right starting from an initial time, t_0: $A_{t_0}B_{t_1}C_{t_2}$.

The algorithm starts by choosing s_0 from the possible values for an $\mathcal{N}$ state system. The weight is $w_{s_0} = \mathcal{N}^2$. Choose (R, P) from the absolute value of the initial density matrix $|\rho_W^{s_0'}(R, P)|$ and record the sign of the density matrix, σ_ρ. Initialize $Z = \sigma_\rho w_{s_0}$.

Propagate (R, P) with the operator $e^{i\mathcal{L}_{s_0}\frac{\delta}{2}}$ to (R', P'), and compute corresponding phase factor W_{s_0}.

Next, compute the matrix elements $(Q_1^2)_{s_0 s_1}$, the probability $P_{s_0 s_1} = \frac{|(Q_1^2)_{s_0 s_1}|}{\sum_{s_1}|(Q_1^2)_{s_0 s_1}|}$, and $D_Q = \sum_{s_1}|(Q_1^2)_{s_0 s_1}|$. Select a matrix element s_1 with probability $P_{s_0 s_1}$, and record the sign of Q_1^2, σ_Q. Compute the change in momentum experienced by the bath if a transition in the bra and/or ket state occured. Of course, if opposite transitions occurred, then there will be no momentum change.

Propagate (R', P') with the operator $e^{i\mathcal{L}_{s_0}}\frac{\delta}{2}$ to $(R", P")$, and compute corresponding phase factor W_{s_1}.

Evaluate $Z = ZW_{s_0}D_Q\sigma_Q W_{s_1}$. Multiply by the value of the observable $O_W^{s_1}(R, P)$.

Repeat with this trajectory until the end time is reached. Repeat with additional trajectories until convergence.

Filters must be used to limit the maximum number of hops and maximum value of the observable to eliminate large biasing fluctuations due to the factors contained in the matrix Q_1. These fluctuations exacerbate the sign problem that comes from the evolution phase factors.

Appendix C

Perturbation theory for quantum critical Bose gas

Here we present the results of a direct perturbative computation of χ_ψ [50]:

$$\chi_\psi(\omega) = \frac{1}{-\hbar\omega + R + \Sigma(\omega)} \tag{C.1}$$

To order U^2, the self energy is obtained by summing the two loop sunset diagram

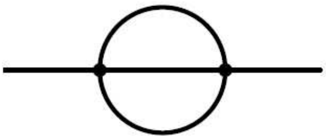

and is given by:

$$\Sigma(i\omega) = -2U^2 \sum_{\epsilon_1,\epsilon_2} \int \frac{d^2k_1}{4\pi^2}\frac{d^2k_2}{4\pi^2}$$
$$\times \frac{1}{(-i\epsilon_1 + k_1^2 + R)(-i\epsilon_2 + k_2^2 + R)(-i(\epsilon_1+\epsilon_2) + i\omega + (k_1+k_2)^2 + R)}.$$

The frequency summation is done most easily by partial fractions and yields

$$\Sigma(i\omega) = -2\left(\frac{U}{k_BT}\right)^2$$
$$\times \int \frac{d^2k_1}{4\pi^2}\frac{d^2k_2}{4\pi^2}\frac{[n(k_1^2+R)-n((k_1+k_2)^2+R)]\,[n(k_2^2+R)-n((k_1+k_2)^2-k_1^2)]}{i\omega+(k_1+k_2)^2-k_1^2-k_2^2-R}.$$

Now we analytically continue to real frequencies, and take the imaginary part at $\omega = R/\hbar$, which is the leading order position of the pole in Eq. (C.1). This yields

$$\begin{aligned} \mathrm{Im}\Sigma(R/\hbar) &= 2\pi\left(\frac{U}{k_BT}\right)^2 \int \frac{d^2k_1}{4\pi^2}\frac{d^2k_2}{4\pi^2}\left[n(k_1^2+R)-n((k_1+k_2)^2+R)\right] \\ &\quad \times \left[n(k_2^2+R)-n((k_1+k_2)^2-k_1^2)\right]\delta((k_1+k_2)^2-k_1^2-k_2^2) \\ &= -2\pi\left(\frac{U}{k_BT}\right)^2 \int \frac{d^2k_1}{4\pi^2}\frac{d^2k_2}{4\pi^2}\left[n(k_1^2+R)-n(k_1^2+k_2^2+R)\right] \\ &\quad \left[n(k_2^2)-n(k_2^2+R)\right]\delta((k_1+k_2)^2-k_1^2-k_2^2). \end{aligned} \tag{C.2}$$

Now we can do the angular integration because the angle appears only in the argument of the delta function, and obtain

$$\begin{aligned} \mathrm{Im}\Sigma(R/\hbar) &= -\left(\frac{U}{2\pi k_BT}\right)^2 \int_0^\infty dk_1 \int_0^\infty dk_2 \\ &\times \frac{(e^{R/(k_BT)}-1)}{(e^{(k_1^2+R)/(k_BT)}-1)(e^{(k_2^2+R)/(k_BT)}-1)(1-e^{-(k_1^2+k_2^2+R)/(k_BT)})}. \end{aligned} \tag{C.3}$$

This result is a function of $R/(k_BT)$ which has to be evaluated numerically. However, it is instructive to examine its value in the classical limit, upon applying the approximation in Eq. (7.20), when we obtain

$$\begin{aligned} \mathrm{Im}\Sigma(R/\hbar) &= -\frac{U^2R}{4\pi^2}\int_0^\infty dk_1 \int_0^\infty dk_2 \frac{1}{(k_1^2+R)(k_2^2+R)(k_1^2+k_2^2+R)} \\ &= -R\left(\frac{U}{R}\right)^2 \frac{(4-\pi)}{16\pi}. \end{aligned} \tag{C.4}$$

Notice that explicit factors of $k_B T$ have dropped out, and consequently Eqs. (C.1) and (C.4) are consistent with the scaling form Eq. (7.9). It is also interesting to compare the value of the classical limit in Eq. (C.4) with that obtained from the full quantum expression in Eq. (C.3). For $R = k_B T/2$ (which are roughly the quasiparticle energy values obtained in the experiments on PHCC [22]), Eq. (C.3) evaluates to a value which is 16% smaller than Eq. (C.4). This gives us an estimate of the error made by representing the quantum-critical theory by classical equations of motion.

Bibliography

[1] I. Affleck. *Phys. Rev. B*, **41**:6697, 1990.

[2] V. Batista and W. Miller. *J. Chem. Phys.*, **108**:498, 1998.

[3] E. Bittner and P. Rossky. *J. Chem. Phys.*, **103**:8130, 1995.

[4] E. Bittner and P. Rossky. *J. Chem. Phys.*, **107**:8611, 1997.

[5] S. Bonella and D. Coker. *J. Chem. Phys.*, **114**:7778, 2001.

[6] S. Bonella and D. Coker. *J. Chem. Phys.*, **118**:4370, 2003.

[7] S. Bonella and D. Coker. *J. Chem. Phys.*, **122**:194102, 2005.

[8] S. Bonella, D. Montemayor, and D. Coker. *Proc. Natl. Acad. Sci. U.S.A.*, **102**:6715, 2005.

[9] G. Ciccotti, B. Berne, and D. Coker (Eds). *Classical and Quantum Dynamics in Condensed Phase Simulations.* World Scientific, Dordrecht, 1998.

[10] D. Dalidovich and P. Phillips. *Phys. Rev. B*, **63**:224503, 2001.

[11] D. Dalidovich and P. Phillips. *Phys. Rev. B*, **66**:073308, 2002.

[12] A. Donoso and C. Martens. *J. Chem. Phys.*, **112**:3980, 2000.

[13] R. Feynman. *Phys. Rev.*, **56**:340, 1939.

[14] D. Fisher and P. Hohenberg. *Phys. Rev. B*, **37**:4936, 1988.

[15] M. Gelfand, R. Singh, and D. Huse. *Phys. Rev. B*, **40**:10801, 1989.

[16] N. Goldenfeld. *Lectures on Phase Transitions and the Renormalization Group.* Perseus, 2002.

[17] M. Hack, A. Jasper, Y. Volobuev, D. Schwenke, and D. Truhlar. *J. Phys. Chem. A*, **104**:217, 2000.

[18] S. Hammes-Schiffer and J. Tully. *J. Chem. Phys.*, **101**:4657, 1994.

[19] E. Heller. *J. Chem. Phys.*, **94**:2723, 1991.

[20] M. Herman and E. Kluk. *Chem. Phys.*, **91**:27, 1984.

[21] J. Hertz. *Phys. Rev. B*, **14**:1165, 1976.

[22] T. Hong, E. Dunkel, S. Sachdev, M. Kenzelmann, M. Stone, M. Bouloubasis, C. Broholm, and D. Reich. *to appear.*

[23] R. Kapral. *Annu. Rev. Phys. Chem.*, **57**:129, 2006.

[24] R. Kapral and G. Ciccotti. *J. Chem. Phys.*, **110**:8919, 1999.

[25] K. Kay. *J. Chem. Phys.*, **101**:2250, 1994.

[26] A. Leggett. *J. Phys.: Cond. Mat.*, **14**:R415, 2002.

[27] A. Leggett, S. Chakravarty, A. Dorsey, M. Fisher, A. Garg, and M. Zwerger. *Rev. Mod. Phys.*, **59**:1, 1987.

[28] Z. Ma. *PhD Thesis*, 2007.

[29] D. MacKernan, G. Ciccotti, and R. Kapral. *to appear.*

[30] D. MacKernan, G. Ciccotti, and R. Kapral. *J. Chem. Phys.*, **116**:2346, 2002.

[31] N. Makri and W. Miller. *Chem. Phys. Lett.*, **139**:10, 1987.

[32] N. Makri and K. Thompson. *Chem. Phys. Lett.*, **291**:101, 1998.

[33] C. McCurdy, H. Meyer, and W. Miller. *J. Chem. Phys.*, **70**:3177, 1979.

[34] P. Meystre and M.Sargent. *Elements of Quantum Optics.* Springer-Verlag, Berlin, 1990.

[35] W. Miller. *Adv. Chem. Phys.*, **25**:69, 1974.

[36] W. Miller. *Faraday Discuss.*, **110**:1, 1998.

[37] W. Miller and C. McCurdy. *J. Chem. Phys.*, **69**:5163, 1978.

[38] A. Millis. *Phys. Rev. B*, **48**:7183, 1993.

[39] T. Moriya and J. Kawabata. *J. Phys. Soc. Japan*, **34**:639, 1973.

[40] A. Oosawa, T. Takamasu, K. Tatani, H. Abe, N. Tsujii, O. Suzuki, H. Tanaka, G. Kido, and K. Kindo. *Phys. Rev. B*, **66**:104405, 2002.

[41] M. Orszag. *Quantum Optics.* Springer, Berlin, 2000.

[42] D. Podolsky, A. Vishwanath, J. Moore, and S. Sachdev. *to appear.*

[43] V. Popov. *Functional Integrals in Quantum Field Theory and Statistical Physics.* D. Reidel, Boston, 1983.

[44] J. Poulsen, G. Nyman, and P. Rossky. *J. Chem. Phys.*, **119**:12179, 2003.

[45] J. Poulsen, G. Nyman, and P. Rossky. *J. Phys. Chem. A*, **108**:8743, 2004.

[46] O. Prezhdo and P. Rossky. *J. Chem. Phys.*, **107**:825, 1997.

[47] N. Prokof'ev, O. Ruebenacker, and B. Svistunov. *Phys. Rev. Lett.*, **87**:270402, 2001.

[48] N. Prokof'ev and B. Svistunov. *Phys. Rev. A*, **66**:043608, 2002.

[49] S. Sachdev. *cond-mat/0401041.*

[50] S. Sachdev. *Phys. Rev. B*, **59**:14054, 1999.

[51] S. Sachdev. *Quantum Phase Transitions.* Cambridge University Press, Cambridge, 1999.

[52] S. Sachdev and R. Bhatt. *Phys. Rev. B*, **41**:9323, 1990.

[53] S. Sachdev and E. Demler. *Phys. Rev. B*, **69**:144504, 2004.

[54] S. Sachdev and E. Dunkel. *Phys. Rev. B*, **73**:085116, 2006.

[55] S. Sachdev, T. Senthil, and R. Shankar. *Phys. Rev. B*, **50**:258, 1994.

[56] K. Schmidt and G. Uhrig. *Phys. Rev. Lett.*, **90**:227204, 2003.

[57] E. Schr´odinger. *Proc. Cambridge Philos. Soc.*, **32**:446, 1936.

[58] S. Sebastian, P. Sharma, M. Jaime, N. Harrison, V. Correa, L. Balicas, N. Kawashima, C. Batista, and I. Fisher. *cond-mat/0502374.*

[59] D. Segale, M. Karavitis, E. Fredj, and V. Apkarian. *J. Chem. Phys.*, **122**:111104, 2005.

[60] Q. Shi and E. Geva. *J. Chem. Phys.*, **118**:8173, 2003.

[61] Q. Shi and E. Geva. *J. Phys. Chem. A*, **107**:9059, 2003.

[62] Q. Shi and E. Geva. *J. Chem. Phys.*, **120**:10647, 2004.

[63] D. Sholl and J. Tully. *J. Chem. Phys.*, **109**:7702, 1998.

[64] G. Stock and M. Thoss. *Phys. Rev. Lett.*, **78**:578, 1997.

[65] G. Stock and M. Thoss. *Phys. Rev. A*, **59**:64, 1999.

[66] G. Stock and M. Thoss. *Phys. Rev. A*, **59**:64, 1999.

[67] M. Stone, C. Broholm, D. Reich, P. Vorderwisch, and N. Harrison. *cond-mat/0503450.*

[68] M. Stone, I. Zaliznyak, D. Reich, and C. Broholm. *Phys. Rev. B*, **64**:144405, 2001.

[69] X. Sun and W. Miller. *J. Chem. Phys.*, **106**:6346, 1997.

[70] X. Sun and W. Miller. *J. Chem. Phys.*, **110**:14, 1999.

[71] X. Sun, H. Wang, and W. Miller. *J. Chem. Phys.*, **109**:4190, 1998.

[72] D. Tannor. *Introduction to Quantum Mechanics: A Time-Dependent Perspective.* University Science Books, Sausalito, 2007.

[73] K. Thompson and N. Makri. *J. Chem. Phys.*, **110**:2823, 1999.

[74] M. Vojta. *cond-mat/0309604.*

[75] A. Walton and D. Manolopoulos. *Chem. Phys. Lett.*, **244**:448, 1995.

[76] H. Wang, X. Sun, and W. Miller. *J. Chem. Phys.*, **108**:9726, 1998.

[77] U. Weiss. *Quantum Dissipative Systems.* World Scientific, Singapore, 1999.

[78] N. Yu, C. Margulis, and D. Coker. *J. Phys. Chem. B*, **105**:6728, 2001.

[79] V. Zapf, D. Zocco, M. Jaime, N. Harrison, A. Lacerda, C. Batista, and A. Paduan-Filho. *cond-mat/05005562.*

[80] J. Zinn-Justin. *Quantum Field Theory and Critical Phenomena.* Clarendon Press, Oxford, 2002.